Synergetic effect of absorber and condenser nano-coating on evaporation and thermal performance of solar distillation unit for clean water production

Amrit Kumar Thakur[a*], Ravishankar Sathyamurthy[a*], R. Velraj[b], R. Saidur[c], I. Lynch[d], Meenakshi Chaturvedi[b], Swellam W. Sharshir[e]

[a] Department of Mechanical Engineering, KPR Institute of Engineering and Technology, Arasur, Coimbatore, Tamil Nadu 641407, India

[b] Institute for Energy Studies, Anna University, Chennai, 600025, Tamilnadu, India

[c] Research Centre for Nano-Materials and Energy Technology (RCNMET), School of Engineering and Technology, Sunway University, No. 5, Jalan Universiti, Bandar Sunway, Petaling Jaya, 47500 Selangor Darul Ehsan, Malaysia

[d] School of Geography, Earth and Environmental Sciences, University of Birmingham, Edgbaston, B15 2TT Birmingham, UK

[e] Mechanical Engineering Department, Faculty of Engineering, Kafrelsheikh University, Kafrelsheikh, Egypt.

*Corresponding author

Amrit Kumar Thakur, Department of Mechanical Engineering, KPR Institute of Engineering and Technology, Arasur, Coimbatore, Tamil Nadu 641407, India, amrit1@gmail.com

Ravishankar Sathyamurthy, Department of Mechanical Engineering, KPR Institute of Engineering and Technology, Arasur, Coimbatore, Tamil Nadu 641407, India, raviannauniv23@gmail.com, ravishankars05@outlook.com

Abstract

Two design modifications to increase the evaporation/condensation and freshwater yield of conventional solar stills (CSS) are presented – absorber coating with black paint (BP) in which

10 wt. % reduced graphene oxide (rGO) was dispersed, and use of a nano-silicon-coated glass cover alongside the rGO coated absorber. Water contact angle analysis revealed that the hydrophilic glass/condenser hindered water droplet movement, whereas the hydrophobic silicon-coated glass enabled significantly faster water droplet movement. The rGO-coated absorber SS, with 99.8 % solar absorptivity, improved the average water temperature by 11 % leading to an augmented full-day freshwater yield of 3031 mL (versus 2160 mL for the CSS). The synergistic effect of the nano-silicon-coated glass and rGO-coated absorber further enhanced the full-day freshwater yield to 3410 mL. Energy/exergy analysis demonstrated enhanced efficiencies of the combined condenser and absorber coated SS of 37 % (energy) and 112 % (exergy), compared to the CSS. Non-linear characteristic equations described the instantaneous gain in energy efficiency of the combined absorber and condenser coated SS. Absorber/basin exhibited the highest rate of irreversibility in all three SS. The cost of water was 0.01 $/L for the dual-modified still. Water physicochemical quality analysis before and after desalination revealed that the purified water was suitable for drinking.

Keywords: *Desalination, Absorber and condenser nano-coating, Water droplet movement, Thermal performance, Water quality*

1. Introduction

With increasing population and industrialization, shortage of potable water is becoming a significant challenge globally in this era. It is estimated that with the current water usage rate, 57 % of people worldwide will be living in area where there is at least one month of water scarcity every year by 2025 [1]. With 97.5 % of the water on earth being salt water, technological advancement and significant research efforts have led to substantial progress in water desalination technologies to achieve fresh water from brackish/sea-water [2]. Different distillation methods,

such as reverse osmosis (RO) and multi-flash have been developed for large-scale water desalination, and are being widely utilized in urbanized societies, although these techniques have major limitations including high fabrication costs, usage of high-grade energy for operation [3] and higher production of the rejected brine as compared to solar based desalination systems [4]. It is estimated that the generation of 22 million m^3/day of clean water needs around 203 metric tons of oil/year [5].

Solar desalination is considered as the oldest water purification method utilized by mankind and presently is an excellent solution globally, especially in low-income countries with abundantly available solar energy. Among the solar desalination methods that have been developed, the solar still (SS) is the lowest-cost desalination device [6]. It is a viable solution to replace high grade energy operated desalination units, as it is completely operated by solar energy, leading to significant reductions in air-pollution and greenhouse gas emissions. Nevertheless, the main limitations of the device are low water yield and efficiency. The freshwater yield and overall performance of SS can be improved by augmenting the rate of vaporization-condensation. Recently, different modifications in design, through active methods, have been used in conventional SS to enhance the water production of the desalination device through incorporation of photovoltaic and photovoltaic thermal components into the SS, pre-heating of the feed-water supply through use of V-shape concentrators [7], use of parabolic concentrators [8] or solar ponds [9] and cooling of the glass cover (to drive condensation) through water/air films and/or introduction of a thermo-electric module [10]. However, active methods commonly drive-up the installation and running costs of the SS unit, so investigators have focused on passive methods to cut costs.

With pioneering advances in material science and nanotechnology in recent years, research has focused on improving the water generation potential of SS using coatings on the absorber and condenser to facilitate both evaporation and condensation. As absorber coatings, nano-SiO_2, nano-TiO_2, micro Cu, Al, and Sn were most widely used to date [11-15] to enhance the solar absorptivity and thermal performance of the SS. The nanoparticles coated surfaces exhibited excellent conductivity and increased the water generation rate of SS. As condenser coatings, Khanmohammadi and Khanjani [16] used cold plasma coating on the glass to change the condensation behavior, and the results illustrated an increased contact angle between droplets of water and the plasma-treated glass as a result of the increased glass hydrophobicity. The plasma-coated glass SS exhibited a water yield of 610 mL, whereas it was only 485 mL for the bare glass SS. Zanganeh et al. [17] studied the effect of glass coating on the performance of an SS using silicon nanomaterials through 'dip' coating. It was found that a silicon coating on the glass enhanced the water yield by 20 %, in comparison with a bare glass SS, by increasing the contact angle of the glass surface after coating, which led to a hydrophobic surface and produced more condensate water then the bare glass.

It is inferred from the above literature summary that surface coating of the glass cover or the absorber improves the water production and performance of the distillation unit. However, the potential synergetic effects of glass/condenser and absorber coating on the performance of desalination units has not been explored to date. In addition, the role of surface morphology and wettability in promoting the flow of the condensed water droplets from the inclined condenser cover has not been reported as yet. Therefore, we aimed to develop novel nano-coatings for both the absorber and condenser and to explore their synergetic effects on increasing the performance and water yield of a solar distillation unit. Reduced graphene oxide, with its excellent solar-thermal

conversion properties, high thermal conductivity and high specific surface area has been selected as the coating material for the absorber, while nano-silicon with its superior hydrophobic properties has been selected for the glass cover / condenser coating. The effect of silicon coating on the condensed water droplet movement and the time taken by the bare and coated inclined condenser cover in moving the droplet with different water volume is investigated in detail and presented, and the overall impact of the combined absorber and condenser coating on water yield and system performed are analyzed.

2. Experimental

2.1 Development of reduced graphene oxide-based absorber coating

The absorber plays a very significant part in enhancing the temperature of the water in a SS, with higher water temperatures leading to faster evaporation and thus to higher water productivity, and therefore the selection of the absorber coating material is very important. The absorber functions to absorb the falling solar radiation and transfers the energy into the adjacent water thereby heating it, and thus, any coating for the absorber must possess excellent solar absorption behavior along with superior solar-thermal conversion behavior. Reduced graphene oxide (rGO) exhibits excellent photo-thermal conversion, high surface area and superior conductivity [18].

2.1.1 Synthesis of rGO and its characterization: - Initially, natural graphite powder (NGP) was converted into graphite oxide by a modified Hummers and Offeman's method [19]. In a Borosil glass beaker, NGP (8 gm), NH_4NO_3 (8 gm) and H_2SO_4 (368 mL, 98 % w/w) were added, and the mixture was homogeneously mixed using a stirrer for 60 min. Thereafter, $KMnO_4$ (40 g) was added to the mixture slowly with stirring over 60 min, leading to a green colored solution. Next, the glass beaker was maintained at a constant temperature of 35 °C, and the solution was stirred using a

magnetic stirrer for 60 min to produce a thick paste. Then, double distilled water (DW) of high purity (640 mL) was poured into the paste and stirred for 60 min at 90 °C, leading to a change in the solution colour from green to brown. Then, DW (1.6 L) was added, followed by H_2O_2 (48 mL), leading to change in solution color to yellow from dark brown. The solution was filtered, followed by washing with aqueous 10 % HCl solution (3.2 L) for removal of the metal ions and was then thoroughly washed using DW numerous times until the solution pH became 6. The resulting graphene oxide (GO) was dried for 24 hours at 45 °C and the structure of the GO powder was analyzed using X-ray diffraction (XRD). The GO was reduced to rGO using the following method.

Firstly, 1 gram of GO was dispersed in 100 mL double DW and sonicated using a probe sonicator for 15 min for homogeneous mixing of the solution. Then 5 mL NH_4 OH (ammonium hydroxide) and 5 mL of H_6N_2O (hydrazine hydrate) were added into the GO solution, and stirred at 30 °C for 30 min. The mixture was heated in a water bath to 90 °C for 45 min under constant stirring. Ultimately, the solution turned dark, which confirmed the reduction of GO into rGO.

Graphite powder, GO, and reduced-GO XRD spectra are presented in Fig. 1 (a-c). For graphite at $2\Theta = 26°$, a sharp diffraction peak appeared that affirms the presence of the graphite phase [20]. This narrow peak confirms the excellent purity of the graphite, its highly crystalline form, and negligible mineral impurities [21]. In is clearly observed that in GO the 'major-peak' has shifted as compared to graphite, which signifies the interlayer expansion of graphite. It also revealed that the method used for synthesis is suitable for producing highly oxidized GO from the graphite. At $2\Theta = 10.9°$, GO demonstrates the major peak [22]. This peak was mainly observed owing to the reduction in the crystal size into nano-size during the preparation and conversion of graphite into GO. Further, in the XRD analysis of rGO, the peak was at $2\Theta = 25.02°$ along with a corresponding interlayer space of 0.34 nm, which demonstrates the effective reduction of GO into rGO.
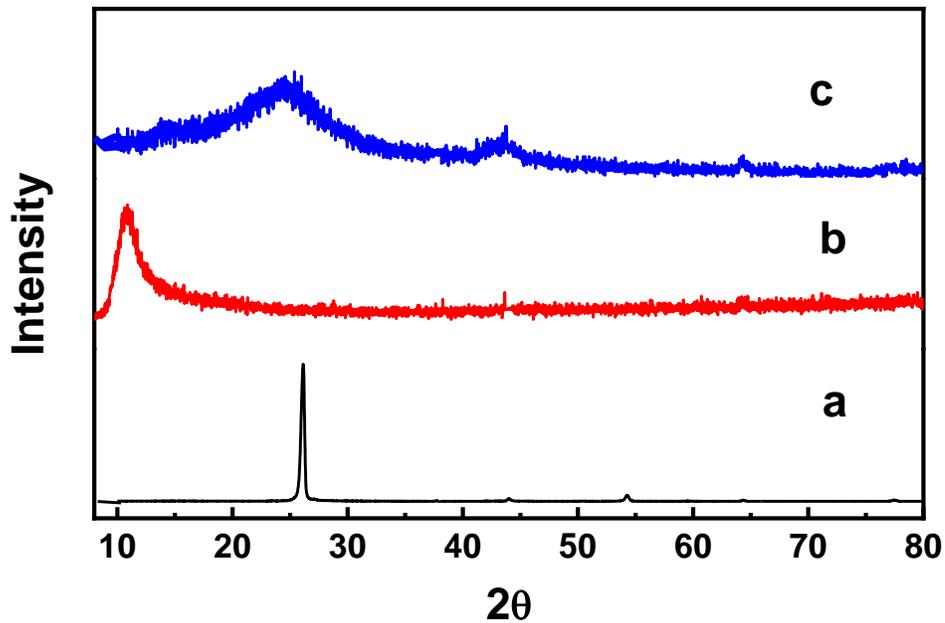
Fig. 1. XRD of (a) the starting graphite, (b) the synthesized GO, and (c) the rGO obtained by reducing the GO.

The peak value of rGO showed that the nanosheets of the rGO were exfoliated into a few layers/monolayer rGO and converted into a novel structure that is considerably dissimilar from graphite and GO [23].
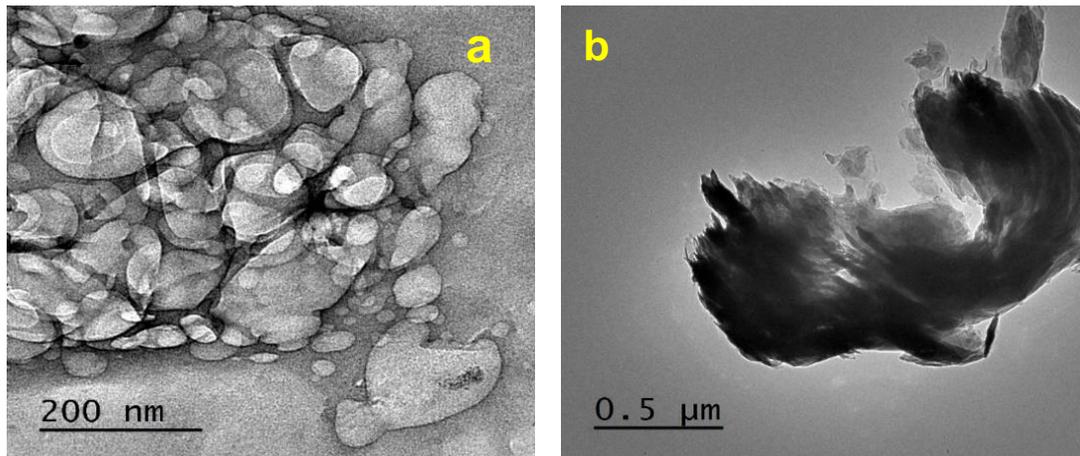

Fig. 2 TEM image of rGO at a magnification of (a) 200 nm, (b) 0.5μm.

Fig. 2 (a-b) depicts the morphology and structure of the rGO using transmission electron microscopy (TEM, JEOL 2100). The rGO sample exhibits a wrinkled and wavy surface due to the overlapping sheets. Brunauer–Emmett–Teller theory (BET) analysis of the rGO is presented in Fig. 3 (a-e).
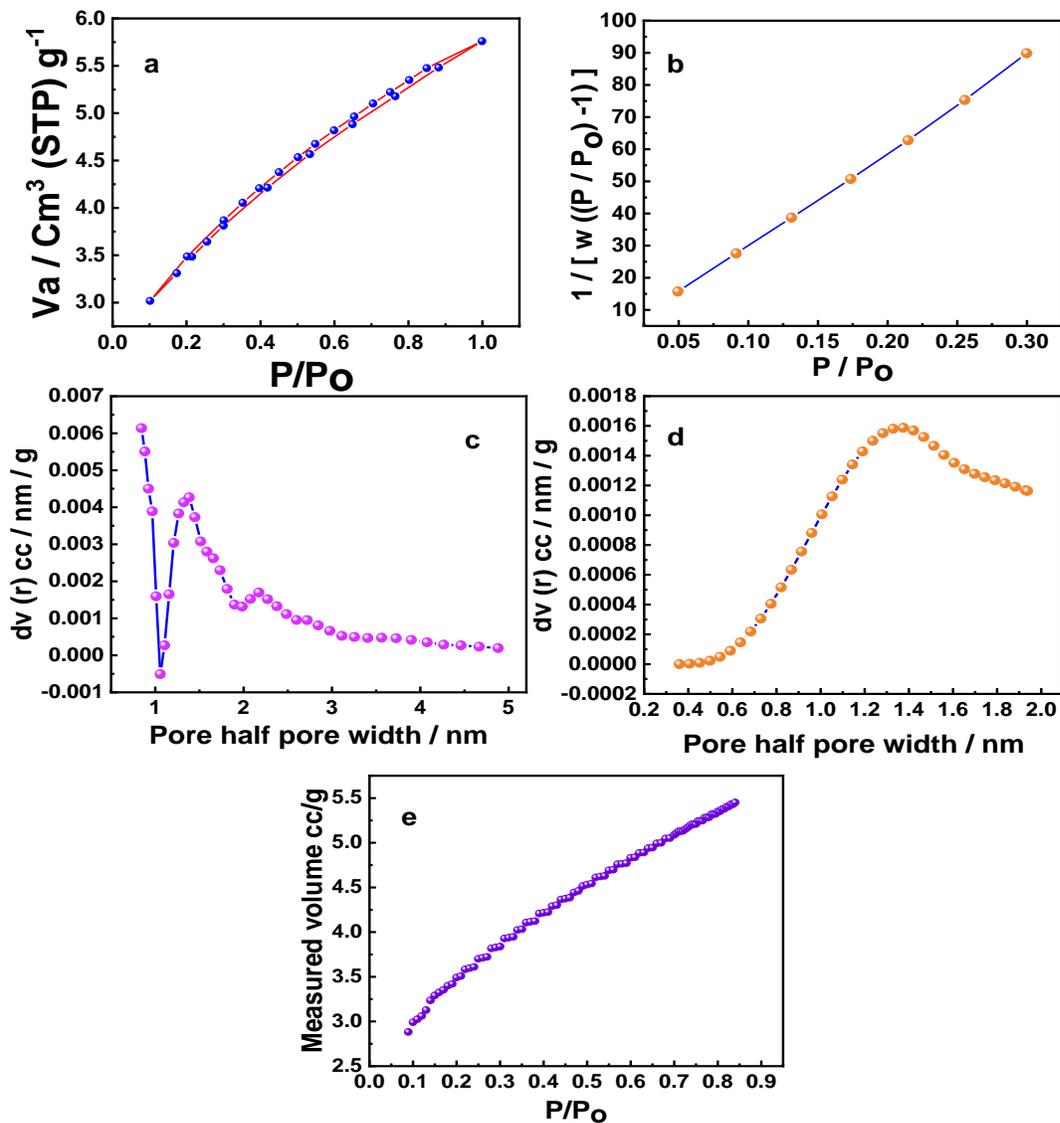

Fig. 3. Surface area analysis of rGO nanosheets: (a) N_2 adsorption/desorption full isotherm curve, (b) BET plot from the N_2 adsorption data (c), DFT method pore size distribution, (d) SF method pore size distribution, and (e) DFT method fitting comparison.

Surface area and pore size for the rGO nanosheets were determined by the nitrogen adsorption-desorption full isotherm and the isotherm loop was of type (IV) with a H1 hysteresis loop ($0.4 < P/P_o > 0.95$). This analysis highlights that the rGO nanosheets have highly uniform pores. The results demonstrated that rGO surface has only 'one type of pore' i.e., mesopores (diameter 2-50 nm). The BET surface area for rGO was 11.8223 m^2/g, and the average pore radius was 1.511 nm.

2.1.2 Preparation of conductive rGO paint coated absorber: After the synthesis and characterization of the rGO, development of a novel rGO based conductive coating for the absorber was carried out. The solar absorber of the desalination unit was made from galvanized iron (GI) (thickness $= 1.6$ mm) with an area of 0.5 m^2. Two different solar absorbers were prepared: (1) using a bare black paint (BP) coating, and (2) using the identical black paint in which rGO (10 wt. %) was dispersed as the coating. Note that 5 and 15 wt. % rGO were also evaluated as noted below, but 10 wt.% provided the optimal functionality.
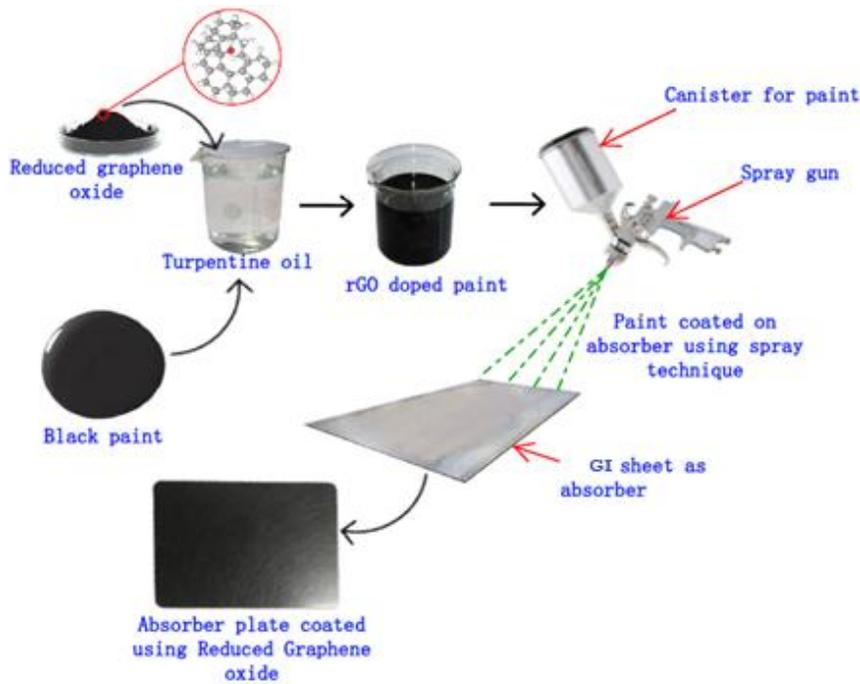

Fig. 4 Scheme for preparation of the rGO coated surface.

A known mass of rGO was dispersed in turpentine: BP mixture (1:4) and the solution was stirred for 30 min. Thereafter, the solution mixture was sonicated for 30 min using a probe sonicator at 15 kHz to achieve a homogenous even solution dispersion of rGO enriched black conductive nano-paint and the detailed schematic diagram for development of the rGO coated surface is depicted in Fig. 4. To verify the presence of rGO dispersion in the paint, XRD analysis of the rGO-modified paint was conducted and presented in Fig. 5. As can be seen, the diffraction peak occurred at 26.87° (002), demonstrating the presence and uniform dispersion of rGO in the paint. For nano-powdered rGO, the peak was exhibited at 25.03° and with the mixing of the rGO into the black paint, it shifted to 25.5° in presence of the black chrome paint. It could be due to the presence of pigments, binders and liquid solvent solvents in the black paint, which has shifted the peak slightly.
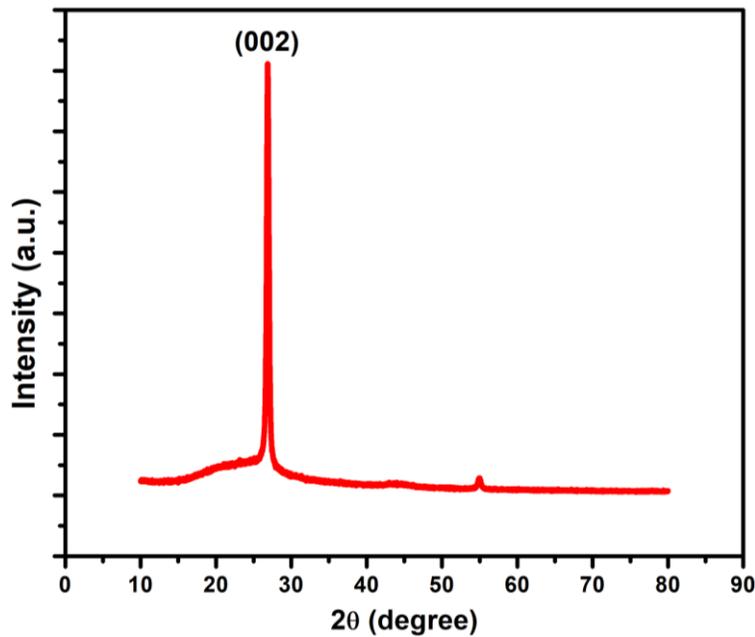

Fig. 5. XRD pattern of rGO-modified paint

Scanning electron microscopy (SEM) images was also analyzed for the rGO dispersed paint, illustrating the uniform dispersion on the rGO in the paint, along with the various sizes of the rGO

sheets as depicted in the red circle in Fig. 6 (a,b). After verification of the distribution of rGO in the paint, the prepared rGO nano-paint was transferred into a spray gun and coated onto the absorber. The conventional bare black paint coated absorber was also coated using a similar method with only the black paint solution (40 mL turpentine and 160 mL black paint mixed homogeneously) sprayed onto the absorber.
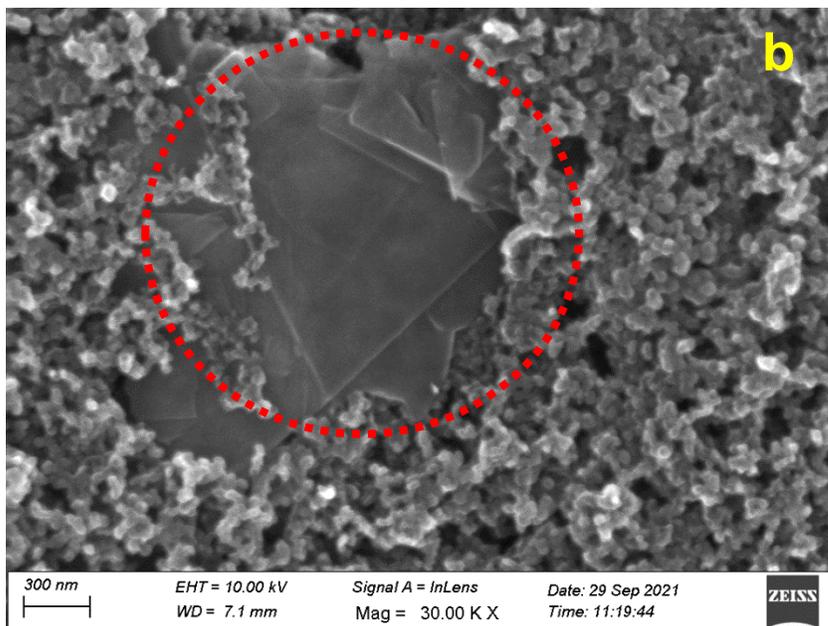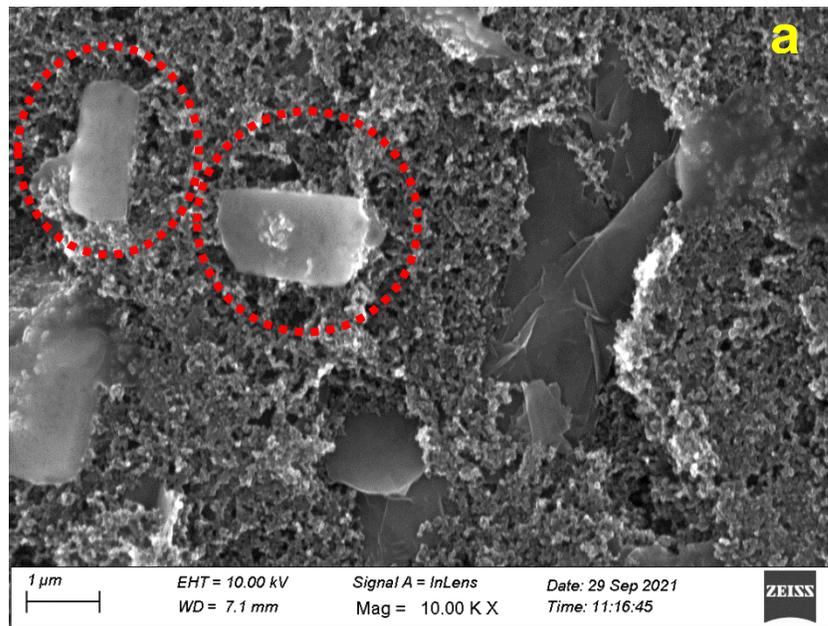
Fig. 6. Scanning electron microscopy images of the rGO-modified paint containing two different particle sizes of rGO in sheet form, and uniformly mixed with the paint, imaged at two different magnifications (c) 1 μm and (d) 300 nm.

Afterward, the prepared absorbers (with and without rGO) were dried under ambient conditions for 72 h and were then used for water heating in the desalination unit. To explore the effect of the rGO mixture in the black paint on the solar absorption behavior, Ultraviolet-Visible Spectroscopy (UV-Vis) analysis was conducted on the bare BP and rGO mixed BP using a Perkin Elmer LAMBDA 950 Spectrophotometer across the wavelength range of 300-1100 nm, and presented in Fig. 7. UV-Vis analysis conducted on the bare BP exhibited 94.2 % average absorptivity of the paint, whereas with 10 wt. % rGO doped into the BP the average absorptivity increased significantly and reached 99.8%. Note that further increasing the wt. % rGO to 15 wt. % did not lead to further enhanced of the absorptivity, and thus 10 wt. % is the optimal loading.
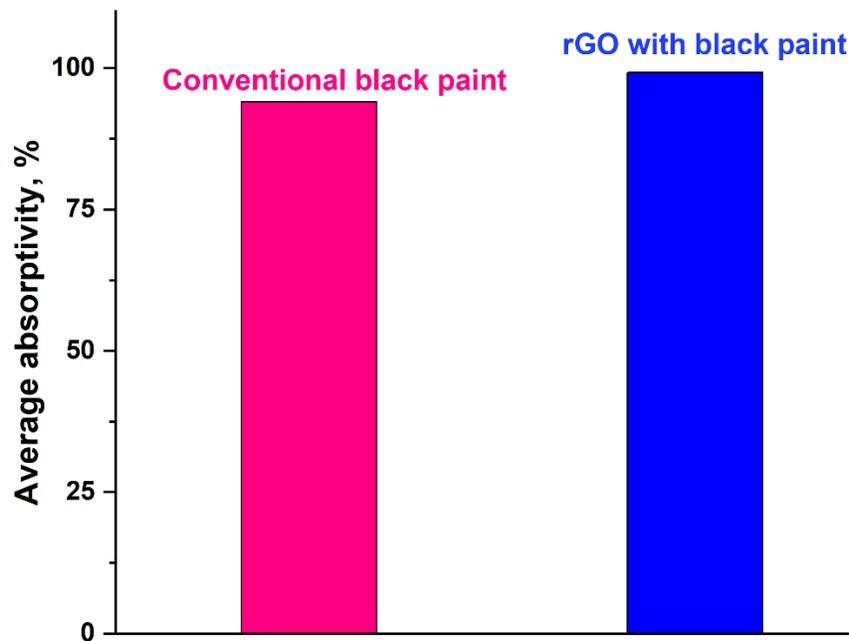

Fig. 7. Average absorption behavior of BP and BP in which 10 wt. % rGO is dispersed

2.2 Development of nano-silicon based glass cover coating

It is well-known that the conventional silica glass used as the condenser cover in desalination units is hydrophilic, which leads to film wise condensation and a reduced heat transfer rate in the still. This behavior of glass reduces the water condensation and significantly affects the productivity of the distillation process. Therefore, an attempt has been made to convert the hydrophilic nature of the glass to a hydrophobic one using the novel transparent coating nano-silicon.
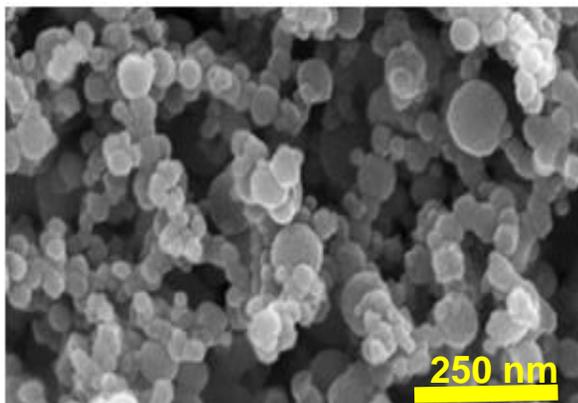

Fig. 8. SEM image showing morphology of nano-silicon

Our group have already developed a similar coating [24] and the same method was adopted to prepare the glass coating. Commercial high-grade nano-silicon was purchased and characterized via SEM. Fig. 8 depicts the SEM image of the nano-silicon and the size of the particles, in the nanoscale, with their spherical structure is clearly visible. Following the characterization of the nano-silicon particles, the development of the glass coating was performed as follows. Extra pure DW (20.7 mL) was mixed with 55.5 mL of tetraethyl orthosilicate (TEOS, 98 %) and the solution was stirred for 180 min at ambient temperature. Separately, 100 mL of ethanol and nano-silicon powder (1.5 gm) were mixed and stirred using magnetic stirring for 30 min and then, the mixture was sonicated for 60 min using a probe sonicator.
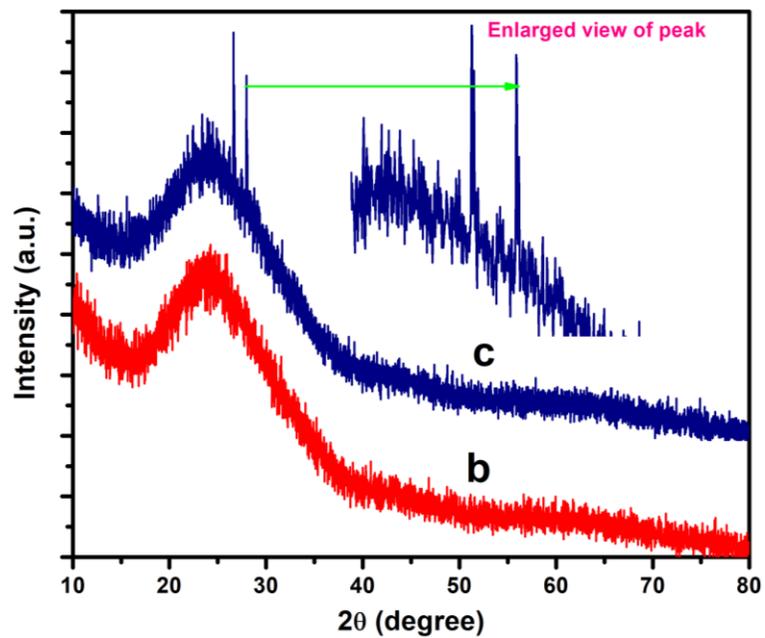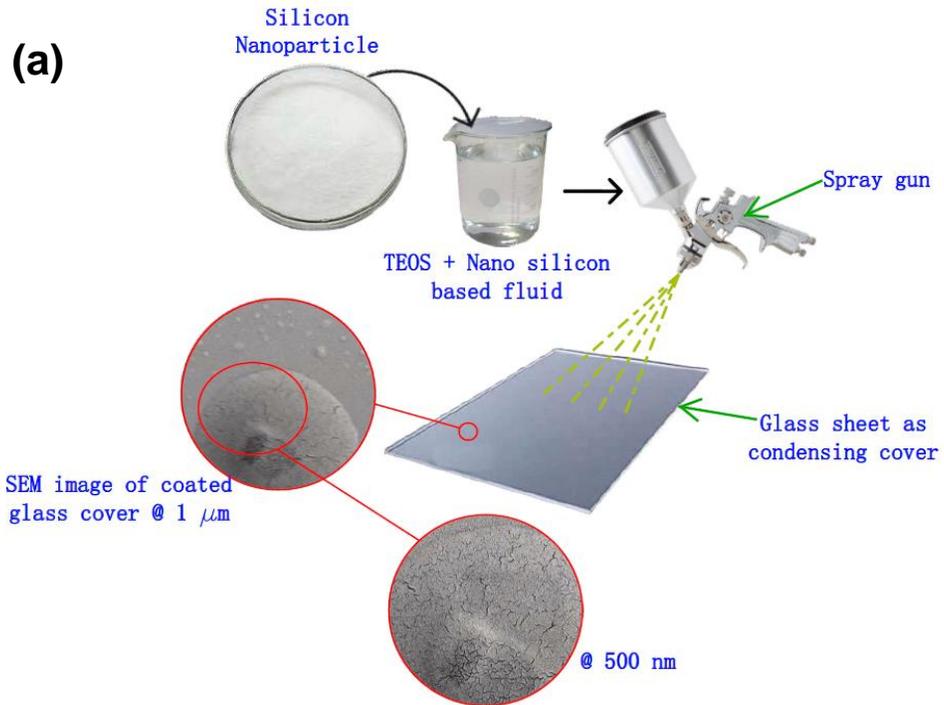
Fig. 9. (a) Schematic representation of the steps involved in the preparation of the nano-silicon glass coated surface. XRD patterns of (b) bare glass, (c) glass coated with nano-silicon; insert: Enlarged view of the peaks in the nano-silicon-coated glass XRD spectrum.

Afterwards, the two solutions were mixed and subjected to magnetic stirring (60 min) and then probe sonication for 120 min. The resulting transparent solution was decanted into the spray-gun and the glass was coated using the solution, dried naturally and subsequently heated at 80 °C to eliminate any trapped solvents, with the schematic for preparation of coated glass including an SEM image of coated surface presented in Fig. 9 (a). To verify the presence of nano-silicon on the coated glass, XRD analysis was carried out and the analyzed pattern is presented in Fig. 9 (b, c). As seen, the broad peak observed at 23.99° (2θ) demonstrated the completely amorphous structure of glass [25]. After coating, the XRD pattern of the coated glass exhibited two different peaks at 27.96° (2θ) and 26.61° (2θ) respectively. The presence of silicon nanoparticle in the coating is verified by the higher peak at 27.96° (111) and similar peak was also reported by Ge et al. [26] for nano-silicon. In addition, one more peak at 26.61° was exhibited by the coated glass, which could be due to presence of residual silica in the form of TEOS which could leads to the peak value of 26.61°. It was inferred that the coated glass exhibited nano-silicon and a small concentration of silica also. After verifying the composition and presence of silicon on coated glass, the surface morphological behavior of the glass with and without coating was examined using commercial atomic force microscopy (AFM, XE-100, Park's systems Inc.) and a 'Dataphysics-OCA 20' contact angle meter (GmbH, Germany) to confirm the conversion from hydrophilic to hydrophobic based on the movement of droplets on the glass surface.

2.3 Experimental test-rig

To explore the synergetic influence of absorber and condenser coating on the SS performance, three different types of SS – (i) bare BP coated absorber SS (CSS) with bare glass condenser, (ii) 10 wt. % rGO doped in BP coated absorber (rGO-CSS) with bare glass condenser, and (iii) 10 wt. % rGO doped in BP coated absorber along with nano-silicon transparent coated

condenser (Si-rGO-CSS) - were fabricated and investigated for their water purification performance under the same weather conditions in Chennai, India (13.0821 °N & 80.2702 °E). Fig. 10 (a) shows a photo of the outdoor experimental test-setup with the conventional and modified SS, while Fig. 10 (b) depicts the schematic arrangement of the proposed solar desalination unit with coated surfaces. The basin of the SS was made from GI and the area of the basin was 0.5 m^2. All walls of basin were painted using BP to facilitate maximum absorption of solar intensity and support increasing water temperature inside the SS. The SS was enclosed at the top through a transparent silica glass of 4 mm thickness. The glass inclination angle is the decisive parameter in determining the water condensate collection and therefore should be chosen carefully. The glass cover/condensate surface was placed on top of the SS in such a manner to attain the tilt angle matching the latitude of the experimental site. The glass was then sealed air-tight with sealant to avoid any water vapour leakage during 'evaporation-condensation'. The exterior walls of the SS were insulated properly using 30 mm thick plywood and the SS was placed onto a thick rubber sheet of 10 mm thickness to avoid any external heat losses. A galvanized iron flow-channel was provided with necessary support for collection of condensate. Three clean glass Borosil^{TM} measuring containers were utilized for measuring the volume of clean water produced with an accuracy of $\pm$ 2 mL. A constant depth of water was kept inside the still basin throughout the experimentation and suitable arrangements were provided for this. The hourly temperature variations of the glass cover, absorber, and water were recoded using k-type thermocouples (Range = 0 ℃ - 100 ℃, and accuracy = $\pm$ 1 ℃). A Solar power meter 'TES-132' was used for solar intensity measurement (Range = 0 W/m^2 to 3500 W/m^2, accuracy = $\pm$ 10 W/m^2). An 'AVM-03' digital anemometer was used for measuring wind velocity (range = 0 - 99,990 CFM, accuracy = $\pm$ 2 %).

The uncertainties in width, length, thickness, and diameter measurements were estimated by the following equation:

$$\delta_N = \sqrt{(\Delta N_1 / N_1)^2 + (\Delta N_2 / N_2)^2 + ... + (\Delta N_n / N_n)^2} \qquad (1)$$

where, N= minimum value and ΔN = range of deviation.

The uncertainty in the above-mentioned measurements are found to be ± 0.5 mm.
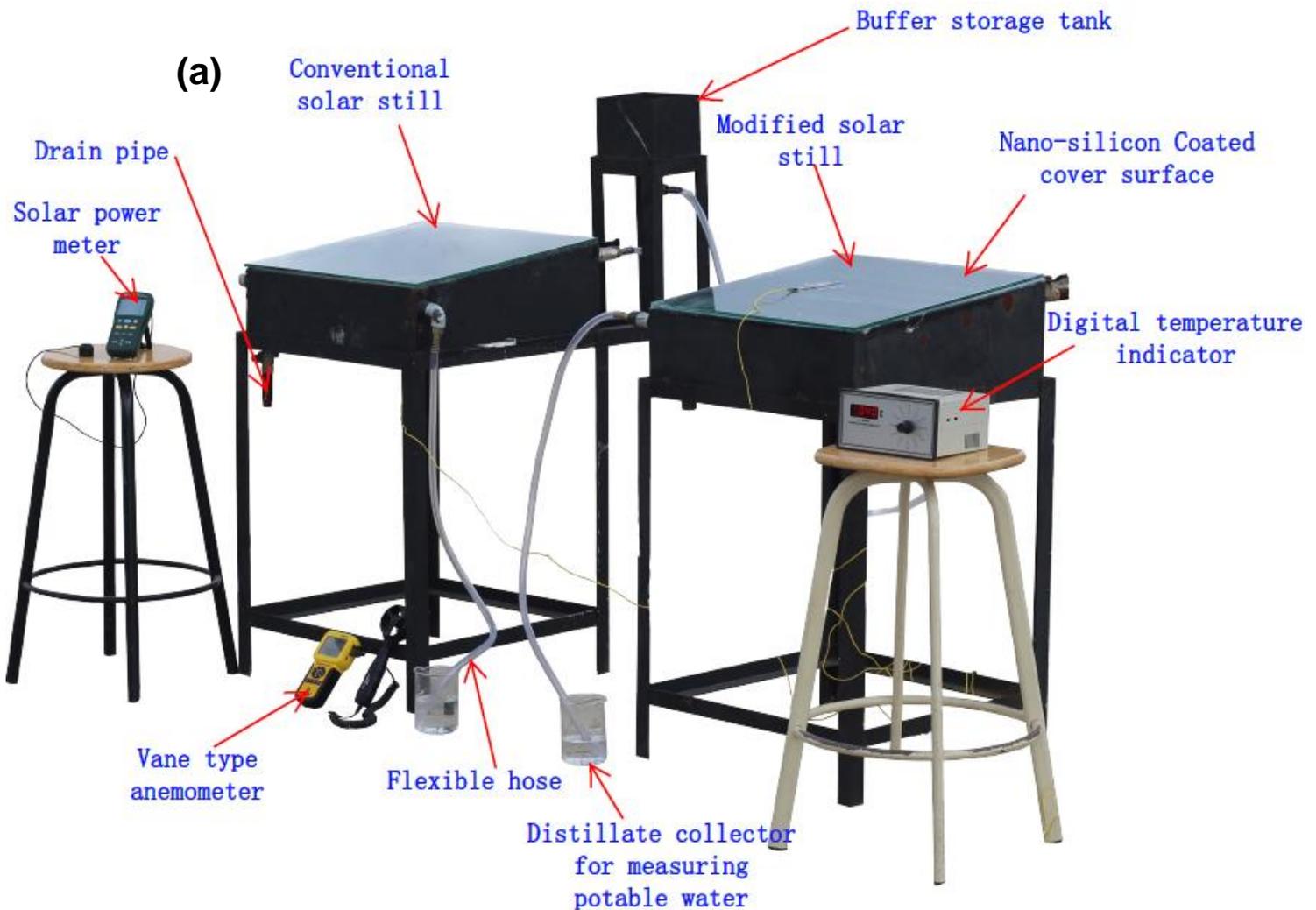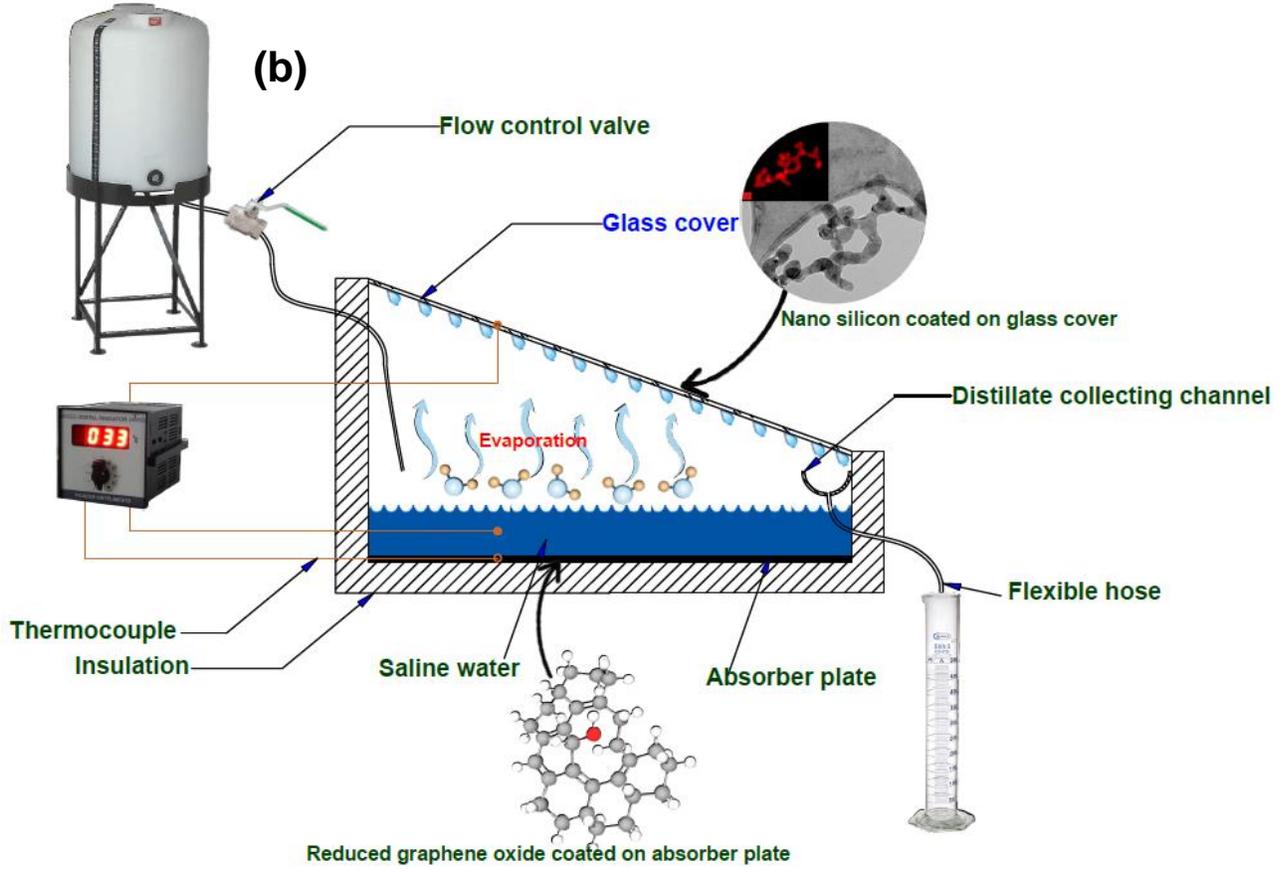
Fig. 10. (a) Outdoor experimental test-setup and (b) Schematic diagram illustrating the

nanocoated condenser and absorber surfaces.

3. Thermal performance of the SS

3.1 Energy efficiency

The energy (η_{energy}) efficiency was determined using Eq. (2), [27]:

$$\eta_{energy} = \frac{m_w \times \lambda_{lg}}{I_t \times A_g \times \Delta t} \qquad (2)$$

where, m_w = water generated by SSs, kg

λ_{lg} = Latent heat of vaporization of water, J/kg

A_{gc} = Area of the SS glass cover, m^2

I_t = Solar radiation, W/m^2

Δt = Time difference, s.

Instantaneous gain in efficiency has also been explored, and expressed using linear and non-linear equations [12]:

For the linear equation,

$$\eta_{e-inst,\ln} = a_1 \left\{ \frac{T_w - T_a}{I_t} \right\} + b_1 \quad (3)$$

where, a_1 and b_1 are the linear constants.

For the non-linear equation,

$$\eta_{e-inst,non-\ln} = a \left\{ \frac{T_w - T_a}{I_t} \right\}^2 + b \left\{ \frac{T_w - T_a}{I_t} \right\} + c \quad (4)$$

where a, b and c are non-linear constants.

3.2 Exergy efficiency

The exergy efficiency was determined using Eq. (5) [28]:

$$\sum E_{x,inp} - \sum E_{x,out} = E_{x,destruction} \quad (5)$$

where, $E_{x,inp}$ = Exergy input

$E_{x,out}$ = Exergy output

$E_{x,destruction}$ = Exergy destruction

The input exergy of the desalination unit is equal to the solar radiation exergy ($E_{x,sun}$), that is determined using following equation;

$$\sum E_{x,inp} = E_{x,sun} = A_{ba\sin} \times I_t \times \left[1 - \frac{4}{3} \times \left(\frac{T_a + 273.15}{T_{sun}}\right) + \frac{1}{3} \times \left(\frac{T_a + 273.15}{T_{sun}}\right)^4\right] \quad (6)$$

where, $T_{ambient}$ = ambient temperature, °C

T_{sun} = sun temperature, 6000 K

A_{basin} = SS basin area, m^2

Exergy output is determined from Eq. (7) [29]:

$$E_{x,out} = E_{x,evap} = \frac{m_w \times \lambda_{lg}}{3600}\left[1 - \left(\frac{T_a + 273.15}{T_w + 273.15}\right)\right] \quad (7)$$

where, T_{water} = temperature of water, °C

The SS exergy efficiency (η_{exergy}) is calculated using Eq. (8):

$$\eta_{exergy} = \frac{E_{x,out}}{E_{x,inp}} \quad (8)$$

3.3 Rate of irreversibility of glass, water and absorber

The calculation involved in determination of the irreversibility for water, glass and absorber/basin utilizes the following equations [30-33]:

The rate of irreversibility ($I_{r,g}$, watts) in glass is calculated using Eq [9], as follows:

$$I_{r,g} = E_{x,g-a} + E_{x,destruction-glass} \quad (9)$$

where, $E_{x,g-a}$ is the rate of exergy loss from the glass to the ambient air (W) and $E_{x,destruction-glass}$ is the exergy destruction in the glass cover (W), determined as follows:

$$E_{x,g-a} = h_{t,g-a} \cdot A_g \cdot \left(T_{g,o} - T_a\right)\left(\frac{T_a + 273.15}{T_{g,o} + 273.15}\right) \quad (10)$$

where, $h_{t,g-a}$ is the total convective heat transfer coefficient between the top glass surface and the ambient air (W/m^2 K), and $T_{g,o}$ (°C) is the outer glass cover temperature.

$$E_{x,destruction-glass} = \alpha_g \cdot E_{x,sun} + E_{xt,w-g} - E_{xt,g-a} \quad (11)$$

where, α_g is the glass absorptivity, $E_{xt,w-g}$ and $E_{xt,g-a}$ are the total exergy destruction between 'water-glass' (W), and 'glass-ambient air' (W), respectively.

$$E_{xt,g-a} = E_{xc,g-a} + E_{xr,g-a} \quad (12)$$

where, $E_{xc,g-a}$ and $E_{xr,g-a}$ are exergy for convection and radiation between 'glass-ambient air' (W) respectively.

$$E_{xc,g-a} = h_{c,g-a} \cdot \left(T_{g,o} - T_a\right)\left(1 - \frac{T_a}{T_{g,o}}\right) \quad (13)$$

$$E_{xr,g-a} = h_{r,g-a} \cdot \left(T_{g,o} - T_a\right)\left[1 + \frac{1}{3} \times \left(\frac{T_a}{T_{g,o}}\right)^4 - \frac{4}{3}\left(\frac{T_a}{T_{g,o}}\right)\right] \quad (14)$$

where, $h_{c,g-a}$ is the convective heat transfer coefficient from glass to ambient air (W/m^2 K) and $h_{r,g-a}$ is the radiative heat transfer coefficient from glass to ambient air (W/m^2 K).

$E_{xt,w-g}$ is the total exergy destruction between water and glass, as determined by:

$$E_{xt,w-g} = E_{x.evap,w-g} + E_{x.conv,w-g} + E_{x.rad,w-g} \quad (15)$$

where, $E_{x.evap,w-g}$, $E_{x.conv,w-g}$, and $E_{x.rad,w-g}$ are the exergy for evaporation, convection and radiation between water and glass (W), respectively, determined as per Equations 16-18:

$$E_{x.evap,w-g} = h_{evap,w-g} \left(T_w - T_{g,i} \right) \left(1 - \frac{T_a}{T_w} \right) \quad (16)$$

$$E_{x.conv,w-g} = h_{conv,w-g} \left(T_w - T_{g,i} \right) \left(1 - \frac{T_a}{T_w} \right) \quad (17)$$

$$E_{x.rad,w-g} = h_{rad,w-g} \left(T_w - T_{g,i} \right) \left[1 + \frac{1}{3} \times \left(\frac{T_a}{T_{sun}} \right)^4 - \frac{4}{3} \left(\frac{T_a}{T_{sun}} \right) \right] \quad (18)$$

where, $h_{evap,w-g}$, $h_{conv,w-g}$, and $h_{rad,w-g}$ are evaporative, convective and radiative heat transfer coefficients between water and glass (W/m^{2}K), respectively. $T_{g,i}$ (°C) is the inner glass temperature.

The rate of irreversibility in water ($I_{r,w}$, W) is determined using following equations:

$$I_{r,w} = E_{x,destruction-water} \quad (19)$$

$$E_{x,destruction-water} = E_{x,b-w} + \tau_g . \alpha_g . E_{x,sun} - E_{xt,w-g} \quad (20)$$

where, τ_g is the glass transmissivity, $E_{x,b-w}$ and $E_{xt,w-g}$ are exergy destruction and total exergy destruction between the 'basin-water' (W), calculated as per Eq. [21]:

$$E_{x,b-w} = h_{c,b-w} \left(T_b - T_w \right) \left(1 - \frac{T_a}{T_b} \right) \quad (21)$$

where, $h_{c,b-w}$ is the convective heat transfer between the basin and water (W/m^{2}K).

The rate of irreversibility in absorber/basin ($I_{r,b}$, W) is determined using equations 22-24:

$$I_{r,b} = E_{x,destruction-basin} \quad (22)$$

$$E_{x,destruction-basin} = \left(\tau_g . \tau_w . \alpha_b \right) . E_{x,sun} - \left(E_{x,b-w} + E_{x,insul} \right) \quad (23)$$

where, α_b is the basin absorptivity, τ_w is the water transmissivity and $E_{x,insul}$ is exergy destruction of insulation (W) calculated as:

$$E_{x,inst} = h_{conv,b-a}\left(T_b - T_a\right)\left(1 - \frac{T_a}{T_b}\right) \quad (24)$$

4. Results and discussion

4.1 Water-droplet interaction and its movement on bare and coated glass-cover

The present work explores the role of hydrophobic and hydrophilic surface interactions with the water droplets formed following condensation, which will be beneficial in analysis of the overall water productivity of the different condenser surfaces. Firstly, to verify the nature of glass before and after the coating, the static water contact angle (WCA) was analyzed for simple glass and the Si-coated glass surface. Using a water quantity of 2 μL, WCA on the bare/plain glass is presented in Fig. 11 (a). The static WCA on bare glass was 62°, demonstrating its hydrophilic behavior. It is important to understand that the surface roughness of glass plays an important part in determination of the WCA and hydrophilicity, as per the 'Wenzel equation' [34], which derived a relationship between the wettability and surface roughness, as shown in Equation 25:

$$\cos\theta_m = r.\cos\theta_Y \quad (25)$$

where, 'θ_m' is the measured contact angle, 'r' presents the roughness ratio and θ_Y represents the 'Young's contact angle'. 'r' is the ratio of the actual to projected solid surface area and it is equal to one for a smooth surface and is > 1 for a rough surface. The roughness analysis of plain glass was done using AFM and is presented in Fig. 11 (b, c). Bare/plain glass exhibited an average roughness (R_a) of 5.75 nm as clearly visible in the three-dimensional topology image (Fig. 11 c). It is obvious that the plain glass surface possesses negligible surface roughness and the surface is

almost smooth, therefore, the measured contact angle and Young's contact angle are same. With the hydrophilic behavior of the bare glass, it is also important to analyse the movement of water droplets formed after condensation. The dripping of the water droplet from the condenser cover is significant in increasing the productivity of the SS and thus, droplet movement was examined by providing the same inclination angle (equal to the actual experimental tilt angle of the glass) to the glass and the water droplet movement is captured using the in-built high image processing camera of 'Dataphysics-OCA 20' contact angle meter (GmbH, Germany). Initially, 10 µL of water was allowed to fall onto the inclined glass and later it was progressively increased to 60 µL, but no major movement of the drop was seen owing to the hydrophilic nature of the glass. Thereafter, 100 µL of water was allowed to fall onto the glass and its movement is presented in Fig. 11 (d). With the large drop size, complete capture of the drop structure was not possible, however the slow movement of the drop is clearly visible in the images. The drop took almost 120 ± 0.1 sec to glide from the center to the bottom of the glass, demonstrating the behavior of the smooth hydrophilic surface. This could be due to the higher adhesive force between the plain glass surface and the water droplet, which restricted the movement of the droplet.


WCA = 62°

Bare Glass

b

Histogram

c

(d)

① 0.25 s
② 20 s
③ 30 s
④ 70 s
⑤ 90 s
⑥ 100 s
⑦ 120 s
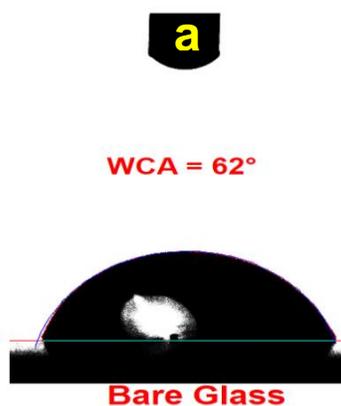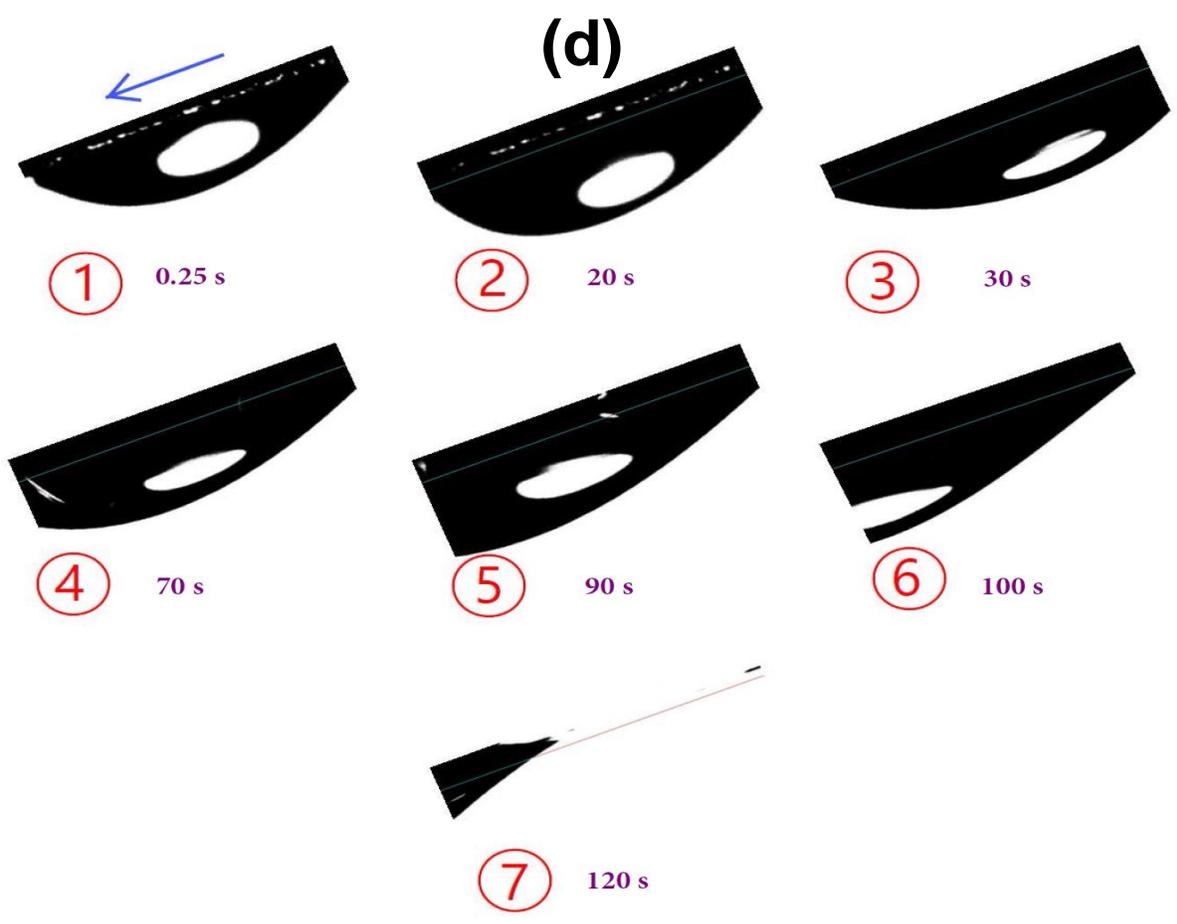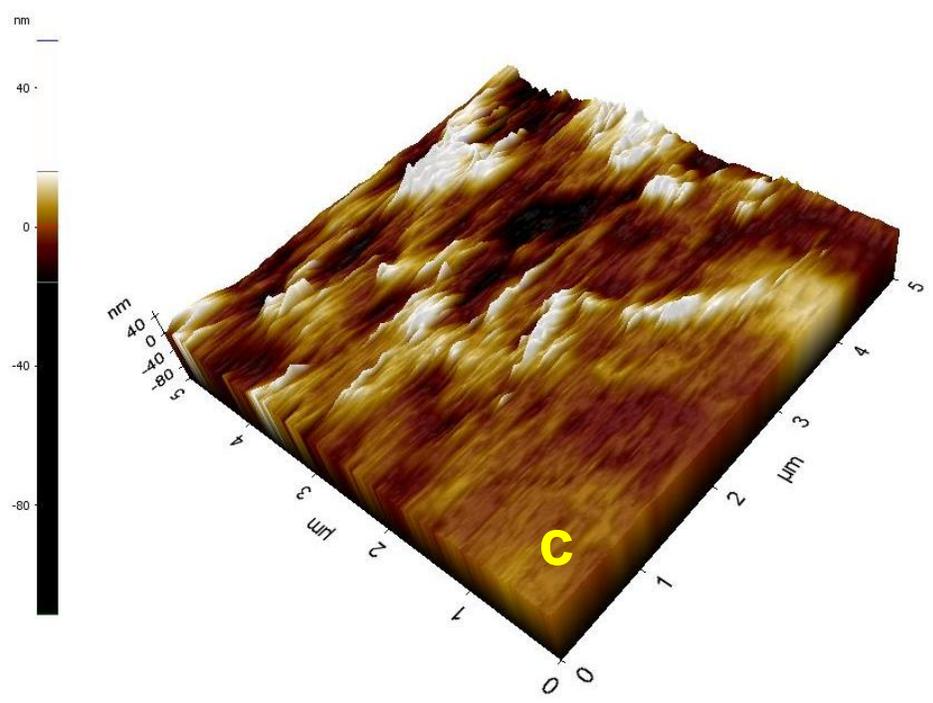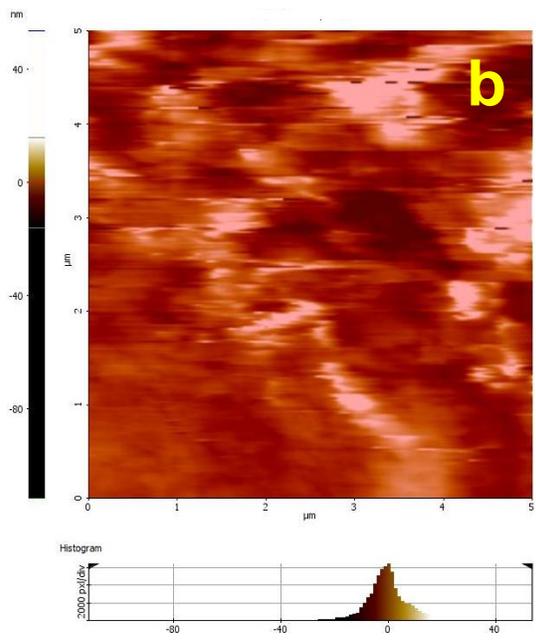
Fig. 11 (a) Static water contact angle on bare glass, (b) 2-D topology and (c) 3-D topology of plain/bare glass determined by AFM. (d) Water droplet movement on inclined plain glass.

WCA = 122°
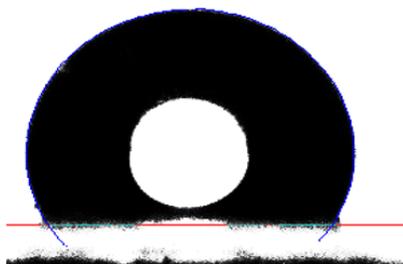
Nano-silicon coated Glass
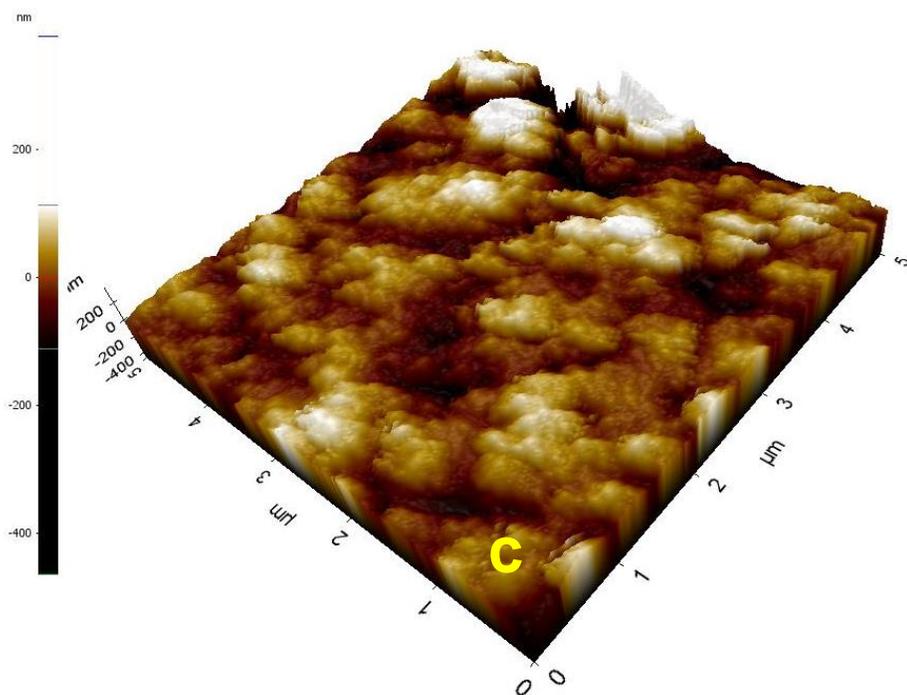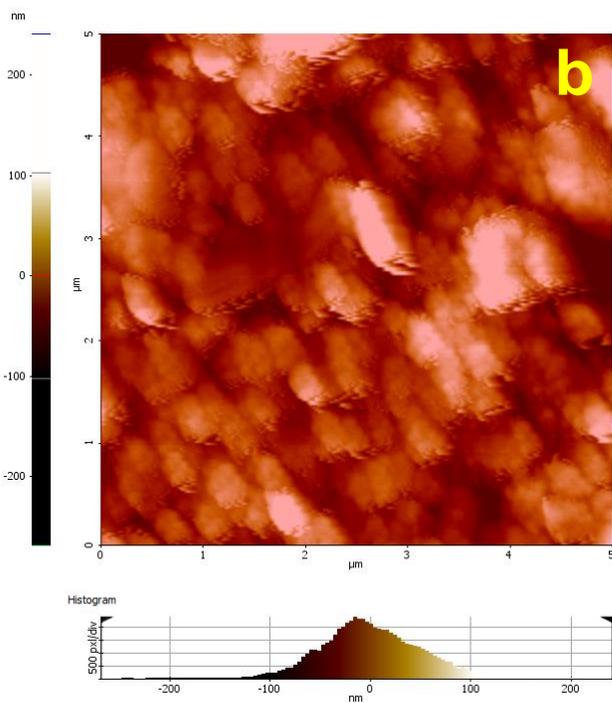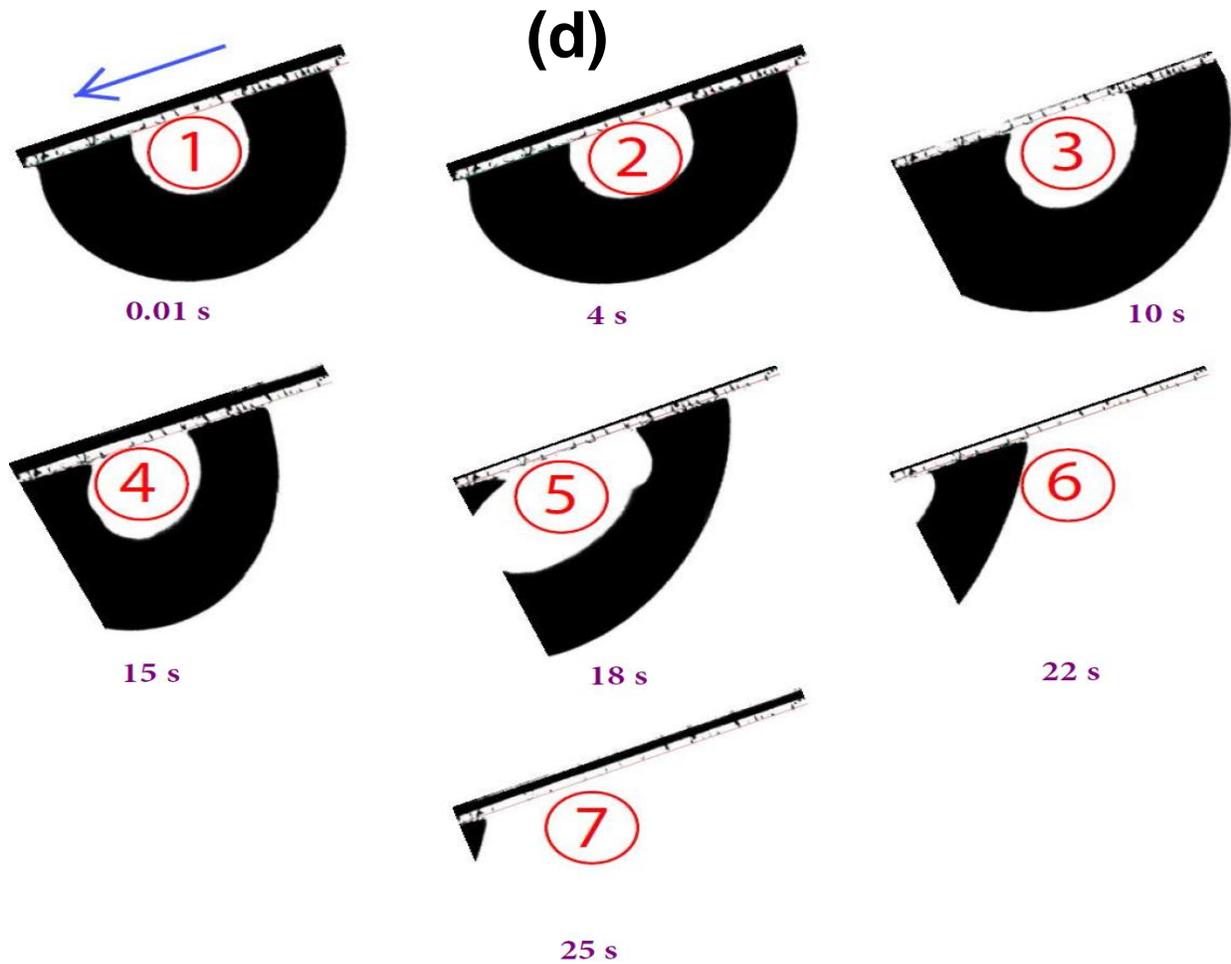
Fig. 12, (a) Static water contact angle on nano-silicon coated glass, (b) 2-D topology and (c) 3-D topology of coated glass, (d) water droplet movement on inclined coated glass.

It is essential to know that the slow movement of the water droplet formed after the water-vapor condensed on the glass hindered the heat transfer rate and adversely affected the freshwater yield generated after collection of the condensed water from the glass cover. Therefore, alteration of the wettability behavior of the glass is indeed needed to improve water droplet movement, which in turn will increase the collection of condensed water from the glass, leading to enhanced water productivity.

With the surface roughness imposed by the nano-silicon, the coated glass surface exhibited a static WCA of 122°, which confirms the alteration of the glass surface nature from hydrophilic to hydrophobic, as presented in Fig. 12 (a). The hydrophobicity could be due to the strong cohesion and weak adhesion between the surface and water along with the lower surface energy of nano-silicon, which prevented the water from penetrating into the micro-pores on the coated surface and increased the WCA [17, 24]. Using the nano-silicon coating, there was a notable change in the surface roughness of the glass and the average roughness was found to be 31 nm, as presented in the 2-D and 3-D topology revealed in Fig. 12 (b, c). The movement of the water droplet on the inclined nano-silicon coated glass is depicted in Fig. 12 (d). With the hydrophobic nature, a water drop of just 60 μL started moving from the center of the glass to the bottom, whereas it required 100 μL on the bare glass. This highlights that with coated glass, even a small water droplet was able to glide from the glass to the collector, thus improving the total water productivity of the SS. As seen in the figure, the water droplet took only 25 ± 0.1 sec to completely move from the center to the bottom of the inclined coated glass, which further demonstrates the role of the hydrophobic coating. The decreased adhesive force between the coated surface and water provided faster movement of the drops, which in turn improved the condensed water movement from the glass and enhanced the water yield.

4.2 Performance studies of SS

The experiments were carried out under Indian climatic condition (Chennai), and the ambient temperature, wind velocity and solar radiation were monitored and are presented in Fig. 13.
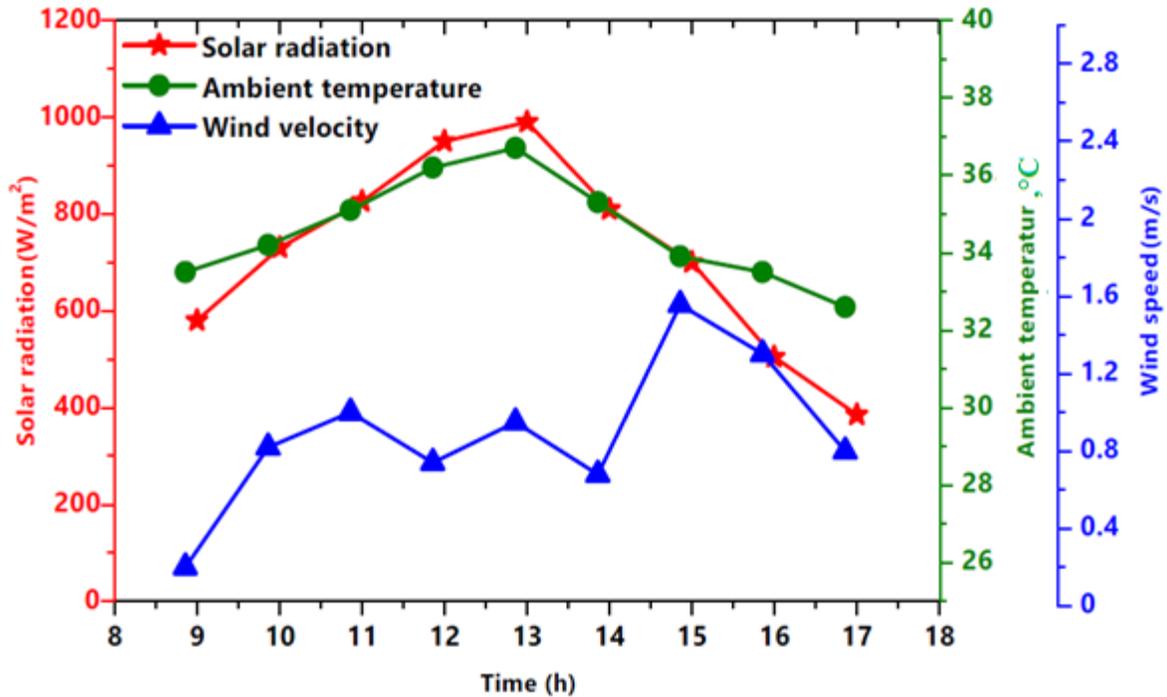
Fig. 13. Solar radiation, ambient air and wind speed variations during the experimentation.

Ambient temperature was measured near to the SS. It is obvious that the wind speed decreases the outer glass temperature, leading to augmented condensation. At the start of the experiments (9.00 AM), solar radiation was 580 W/m² and reached 990 W/m² by noon and then decreased later. The peak ambient temperature was 36.7°C along with an average full day temperature of 34.5°C. The wind velocity (average) was 0.89 m/s. The analysis of the detailed temperature gain, condensation behavior and water productivity of the three SS tested are presented below.

Fig. 14 (a) presents the transient temperature variations during the experiment with the conventional SS with the bare-BP coated absorber. As seen in figure, the highest temperature is exhibited by the absorber among all the measured junctions (i.e., glass and water). The peak temperature of the absorber was 68°C along with average temperature of 56.4°C across the day. The elevated temperature of the absorber increases the brackish water temperature in the still and

leads to a good rate of evaporation. It is also fascinating to note that the bare BP coating on the GI absorber helps in absorbing the maximum possible amount of available incident solar radiation. UV-Vis analysis conducted for the bare black paint showed 94.2 % absorptivity of the paint. Water peak temperature was 65°C along with average temperature of 54.4°C. The increasing water temperature resulted in a higher rate of evaporation of water and the water vapour started accumulating at the inner glass surface. The glass surface peak and average temperatures were 55°C and 47.1°C, respectively. It is well known that the temperature difference between the glass and water is an important parameter, and a larger difference causes greater water condensation which generates a higher volume of freshwater. The highest water-glass temperature difference was 11°C at noon. Conventional glass used as the condenser surface exhibited hydrophilic properties, which is verified using the water contact angle measurement on the glass surface.
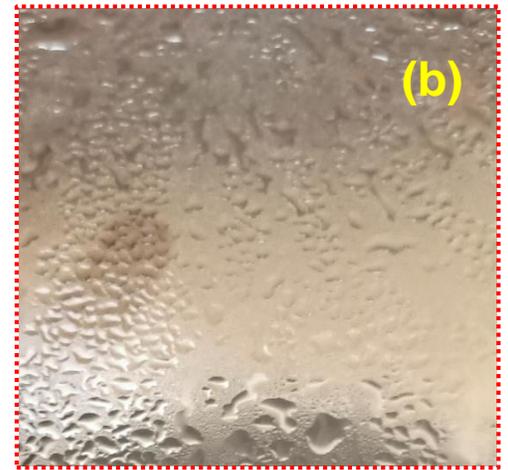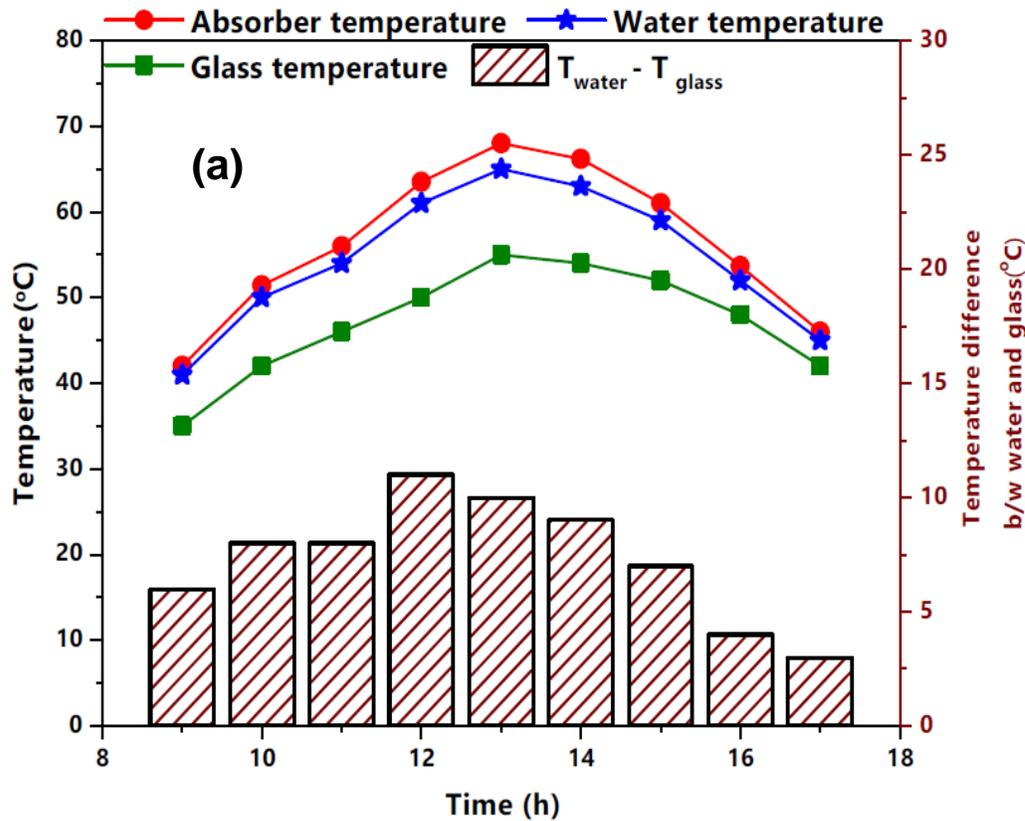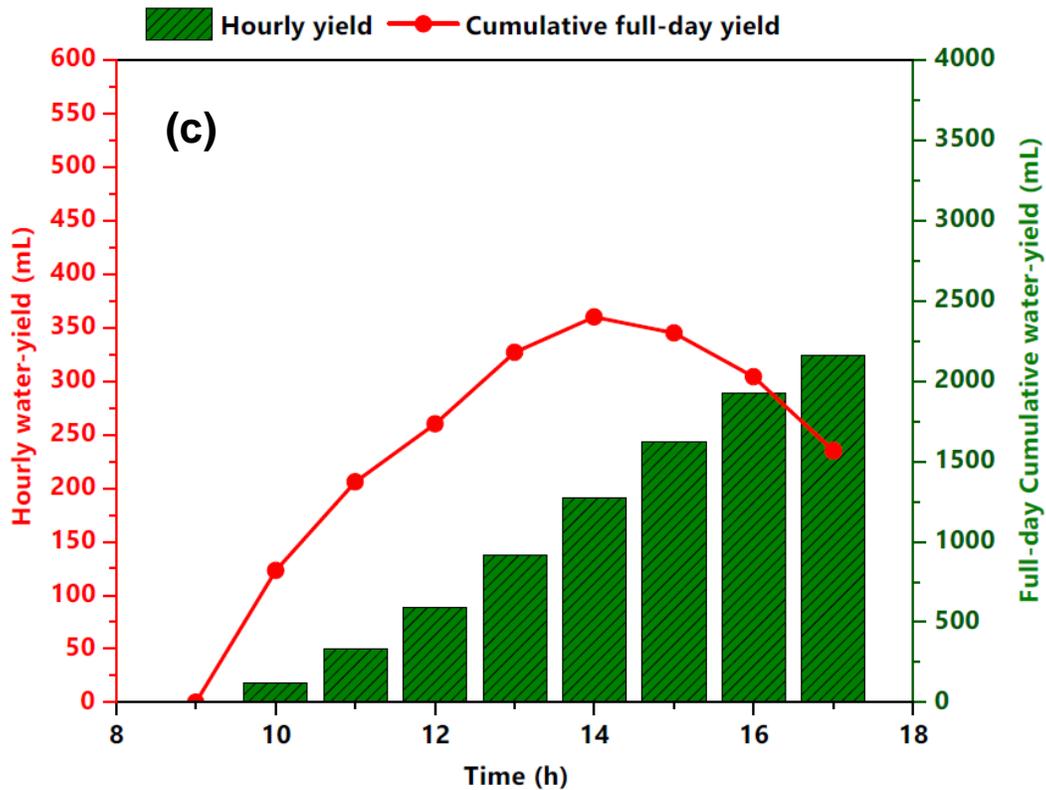
Fig. 14. Performance of the CSS. (a) Transient temperature variation across the absorber, glass and water; (b) A film of condensation formed on the inner glass; (c) Hourly and full-day collective water productivity.

Hydrophilic glass with the designed inclination angle promoted 'film wise' condensation of the water vapor, as illustrated in Fig. 14 (b). As seen in the figure, the smooth glass surface with its hydrophilic nature promoted 'film wise' condensation, which covers the glass with a thin-layer of water and causes higher thermal resistance. This unfavorably affected the water yield of the SS. The maximum hourly productivity and cumulative/cumulative full-day productivity of the CSS were 360 mL and 2160 mL, respectively, as presented in Fig. 14 (c).

To explore the role of the rGO enhanced high conductive BP coated absorber along with a conventional glass surface on water productivity and system performance of the SS, the experiment was repeated. Fig. 15 (a) depicts the transient temperature variation of the rGO-CSS, showing that the rGO-coated absorber exhibited a maximum temperature of 74°C (6°C higher than that of the CSS). This could be a result of the exceptional solar absorption properties and thermal conductivity of rGO. UV-Vis analysis showed 99.8 % absorptivity of the rGO dispersed paint, which provided maximum absorption of the incident solar radiation. The average absorber temperature was also increased relative to the CSS and reached 62.5°C. The increasing temperature of the absorber helps in raising the water temperature and leads to higher evaporation of water vapour. The recorded peak water temperature was 70°C (7°C higher than in the CSS) along with an average of 60.4°C (water). Greater temperature of water generated more vaporized water, which accumulated on the conventional inner glass and increased its temperature. The glass peak and average temperatures were 58°C and 49.3°C, respectively.
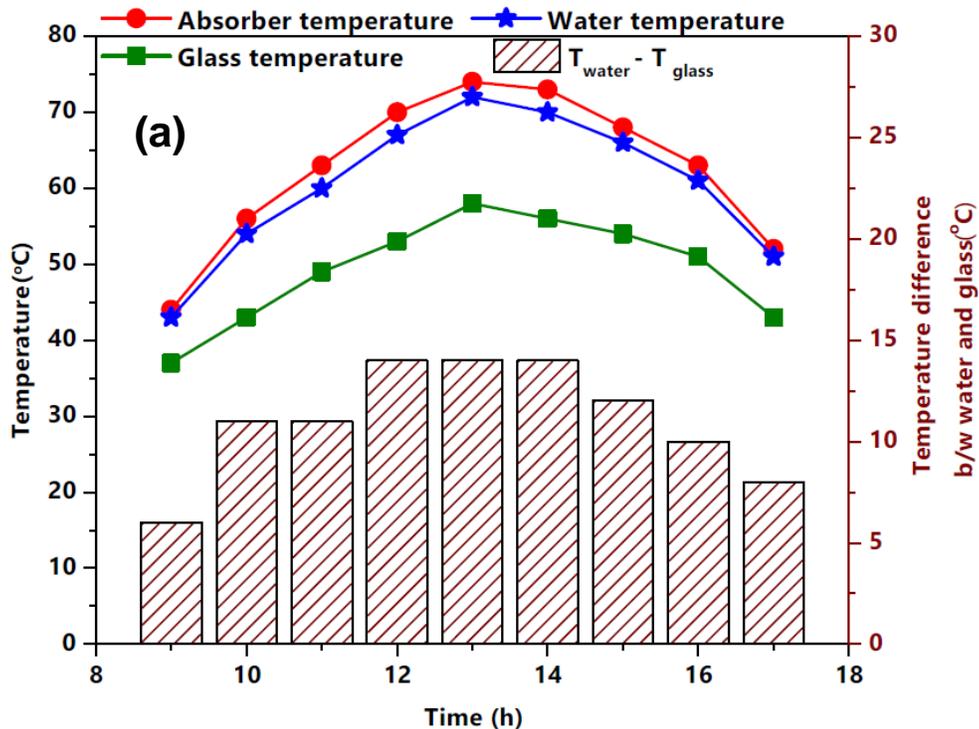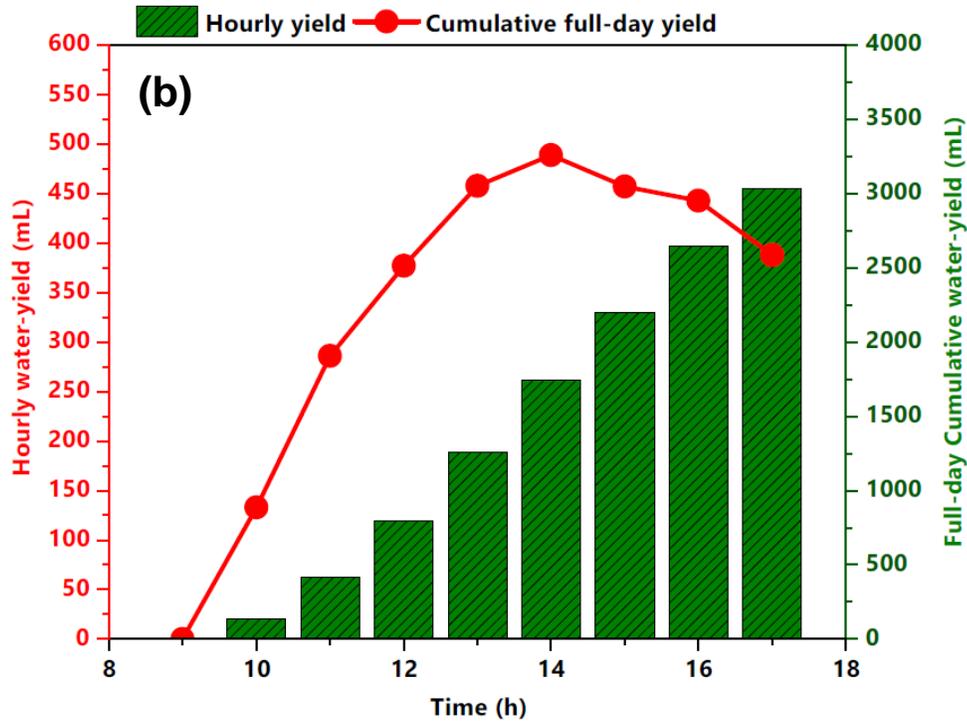
Fig. 15 (a) Transient temperature variation, and (b) hourly and collective full-day water yield of rGO-CSS.

In addition, there was a significant increase in temperature difference between the water-glass after coating of the absorber with the rGO-dispersed paint, and it reached a maximum of 14°C, while only 11°C for the CSS. The highly conductive rGO - coated absorber improved the hourly yield which reached a maximum of 489 mL (compared to 129 mL for the CSS), as revealed in Fig. 15 (b). Porosity has previously been demonstrated to influence solar adsorption, facilitating multiple reflection of the incident solar irradiation, which results in higher solar absorption [35]. Similarly, the highly porous structure (with pore size of 10 nm – 550 nm) and large pore size of the rGO dispersed paint provides excellent solar absorption capability to the SS. Additionally, porous structures have been demonstrated to provide heat storage behavior to coated absorbers, enabling storage of the generated solar energy during peak solar radiation hours and its subsequent

Cumulative water yield exhibited after peak solar radiation (2 PM to 5 PM) was only 1244 mL for CSS, whereas it was significantly improved to 1777 mL for the rGO-CSS. The full day cumulative water yield (9 AM to 5 PM) was 3031 mL for the rGO-CSS. It is inferred from the outcomes that the rGO based absorber demonstrated an excellent rate of heat transfer and produced a significantly higher volume of purified water as compared to the CSS.

To explore the potential for a synergetic effect of absorber coating (using rGO) along with coating of the condenser/glass on water productivity of SS, the same experiment was conducted in the combined SS (Si-rGO-CSS). Fig. 16 (a) presents the transient variation in temperature of the Si-rGO-CSS. As the coating on the glass surface was transparent, there was a small effect on absorber and water temperature of the SS, compared to the rGO-CSS. As seen in Fig. 16 (a), the maximum water and absorber temperature were 71.5°C and 74°C, respectively. The nano-silicon coating on the glass surface has significantly increased the water contact angle, confirming that the alteration in the glass surface properties made it hydrophobic. The hydrophobic behaviour of coated glass promotes drop-wise condensation, as seen in Fig. 16 (b). With drop-wise formation of water vapour, there is noteworthy decrease in the glass surface temperature, whose maximum value was found to be 56°C, compared to 58 °C for the rGO-SS. This decreased glass temperature could be due to the faster movement of the water vapour through a straight-line trajectory of the drop-wise condensation, which leads to faster flow of the accumulated vapor towards the water collection point. The straight-line trajectory in drop-wise condensation is evident in Fig. 16 (b). A synergistic effect of absorber coating using rGO and condenser coating through nano-silicon has significantly improved the water productivity of the dual-modified SS, as presented in Fig. 16 (c).
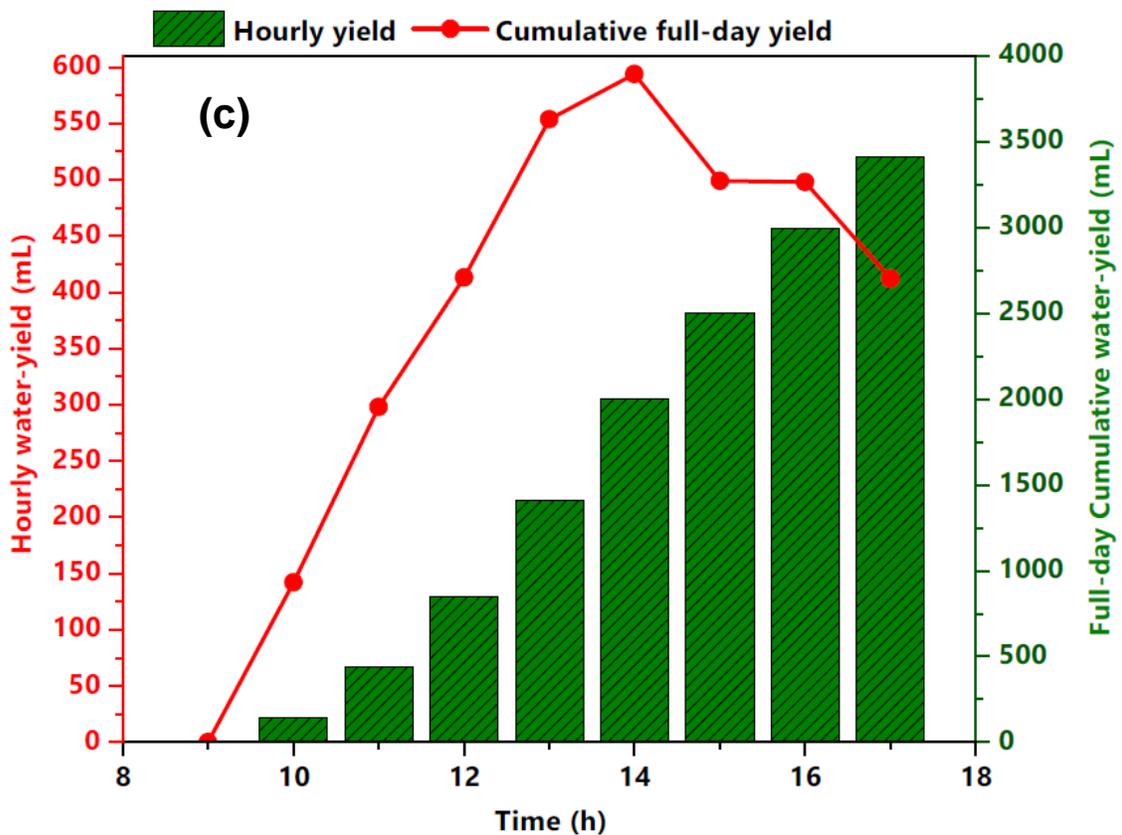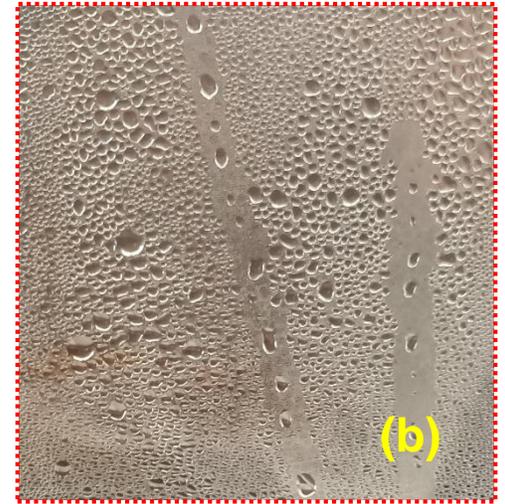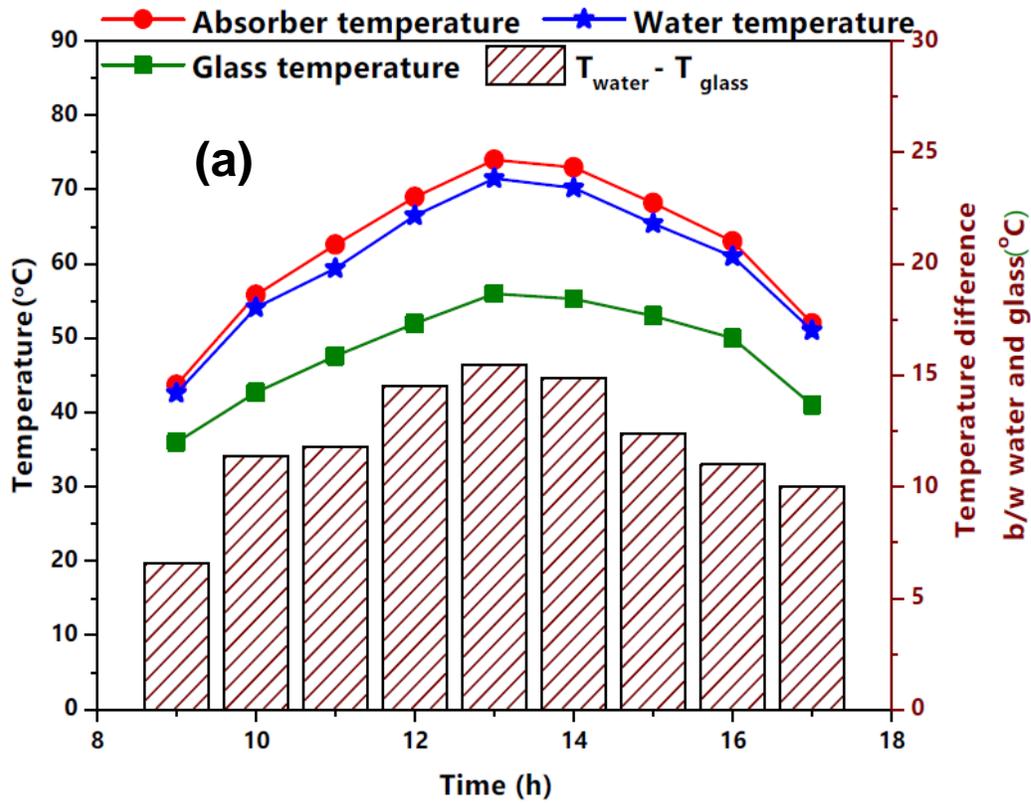
Fig. 16. Performance of the Si-rGO-CSS. (a) Variation in temperature of the coated absorber, coated glass and water; (b) Drop-wise condensation formed on the coated condenser; and (c) hourly and collective full day water productivity of Si-rGO-CSS.

The peak water hourly productivity was 594 mL (65 % higher than the CSS). The dramatic improvement in water yield was generated owing to the exceptional solar absorption properties and conductivity of rGO based absorber coupled with the silicon coated condenser. The Si-rGO-SS exhibited a full-day cumulative water yield of 3410 mL (58 % more than conventional unit). In addition, the collective water yield after peak solar radiation (2 PM - 5 PM) was 61 % higher than the conventional unit. It is inferred from the above results that the altered glass and high conductive absorber coating also promoted higher heat transfer and generated a significantly higher water yield for the SS with the modified condenser and absorber.

4.3 Energy, exergy and irreversibility analysis

The energy efficiency (η_{energy}) of the three SSs is determined using equation (2) and is presented in Fig. 17 (a). The η_{energy} relies on the water output and thus the CSS exhibited an average full-day efficiency of 36.3 %. For the CSS-rGO, the average full day energy efficiency was 44.2 %. With the synergetic effect of the rGO absorber and the nano-silicon coated condenser, the water yield achieved was the maximum from the three stills, and similar behavior was observed in energy efficiency. As seen in Fig. 17 (a), the Si-rGO-CSS exhibited an average energy efficiency of 49.7 %. Hence, utilization of the coated absorber as well as coated condenser provided the highest gain in water yield and leads to the maximum energy efficiency.
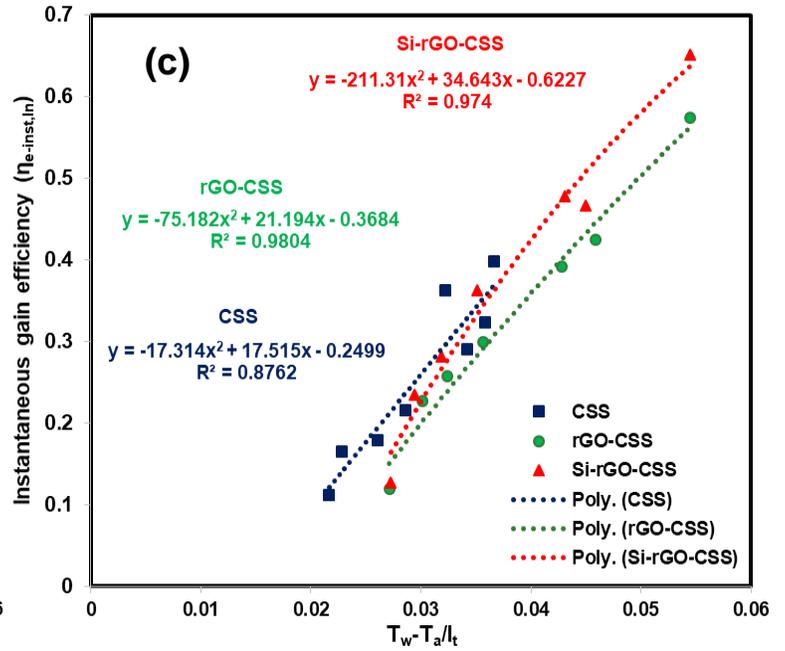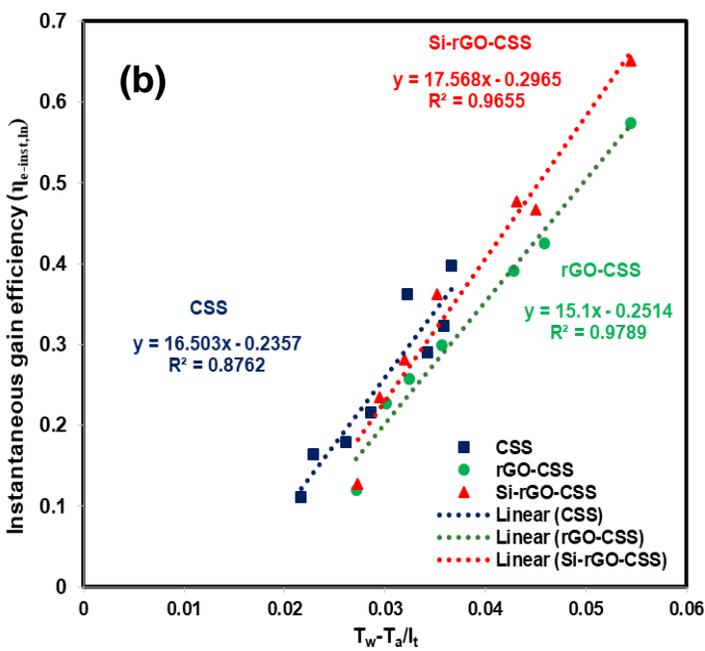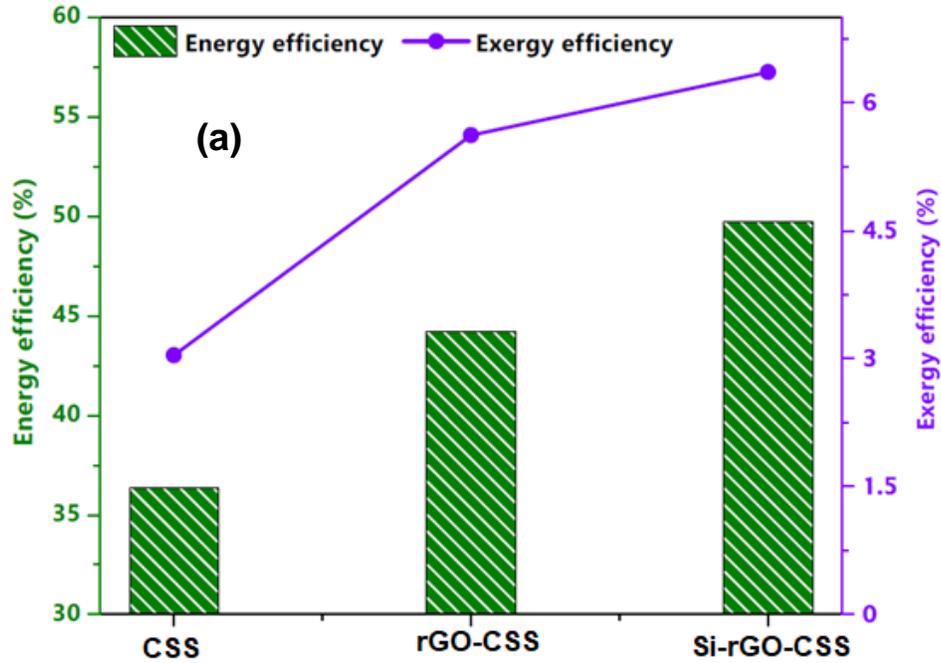
Fig. 17. (a) Full-day average energy and exergy efficiency; (b) Linear characteristic and (c) Non-linear characteristic curve for the instantaneous energy gain for the CSS, rGO-CSS and Si-rGO-CSS.

This work also explored the linear and non-linear characteristic curves for the instantaneous efficiency gain. The two different techniques were used to determine the instantaneous gain efficiency using equations (3) and (4), respectively. Using the linear and non-linear (quadratic) equations, the instantaneous efficiency gain for CSS, rGO-CSS and Si-rGO-CSS were determined and are plotted in Fig. 17 (b-c). Similarly the characteristic equation constants (a_1, b_1 for the linear and a, b, c for the non-linear curves) along with the coefficient of correlation (R^2) are tabulated in Table 1. Fig. 17 (b) depicts the linear characteristic curves along with the developed equations for the instantaneous gain in energy efficiency of the SSs with their coefficients of correlation. One evident point seen from the curves is that the determined instantaneous gain in energy efficiencies are higher than those of Dev and Tiwari [36] for a hybrid (PV-T) active SS which is impressive given that our SSs relies entirely on solar irradiation. This is mainly due to the coating effect which significantly augmented the water yield and the determined values of efficiency. Fig. 17 (c) presents the non-linear characteristic curves along with the developed equations for the instantaneous gain in energy efficiency of the SSs with their coefficients of correlation. As seen in the figure and also clearly in Table 1, the performance characteristic of the non-linear curve is better compared to the characteristic curve generated using the linear equation, based on the respective correlation coefficients, as presented in Table 1.

Table 1. Linear equation and non-linear equation constants and coefficient of regression of instantaneous gain efficiency

Type of SS	Linear equation constants			Non-linear characteristic equation			
	a_1	b_1	R^2	a	b	c	R^2
CSS	16.50	-0.235	0.8762	-17.314	17.515	-0.249	0.8762
rGO-CSS	15.1	-0.251	0.9789	-75.182	21.194	-0.368	0.9804

| Si-rGO-CSS | 17.56 | -0.296 | 0.9655 | -211.3 | 34.643 | -0.622 | 0.974 |

This could be due to the unsteady variation in the climatic parameters, which provides more advantageous conditions for the non-linear (quadratic equation constant) curve than for the linear curve. Similar results of higher performance under the non-linear conditions were also exhibited by Dev and Tiwari [36]. It is also interesting to note that most of their characteristic curve behavior was explored under varying water depths in the desalination unit [36], whereas in the present work emphasis is only on the effect of absorber and condenser modifications in the desalination unit, and further experimentation to vary the water depth is recommended for accurate characteristic curve and equation determination for assessing the instantaneous gain in energy efficiency. With a constant water depth in the present work, higher accuracy was exhibited by the non-linear curve, and equation (4) with suitable constants is recommended as a basis for developing new characteristic equations for coated desalination units in future work.

The full-day average exergy efficiency (η_{exergy}) of the CSS, RGO-CSS and Si-RGO-CSS is calculated using the relationship from equation (8), and the exergy efficiency is revealed in Fig. 17 (a). From this, it is perceived that the CSS exhibited an exergy efficiency of only 3 %. It is obvious that the CSS, without any modification, showed a lower gain in water temperature which is the significant parameter in determination of η_{exergy}. Relatively lower water temperatures leads to lower exergy efficiency. With the solar absorber coating using RGO (RGO-CSS), there was a tremendous improvement in solar absorption behavior of the absorber, which provided optimum heating for the water and significantly improved the water temperature. This leads to an average full day exergy efficiency of 5.6 %. With the synergetic effect of absorber and condenser coating

(Si-RGO-CSS), there was further improvement in the performance of the desalination unit, leading to an improved exergy efficiency of 6.3 %.
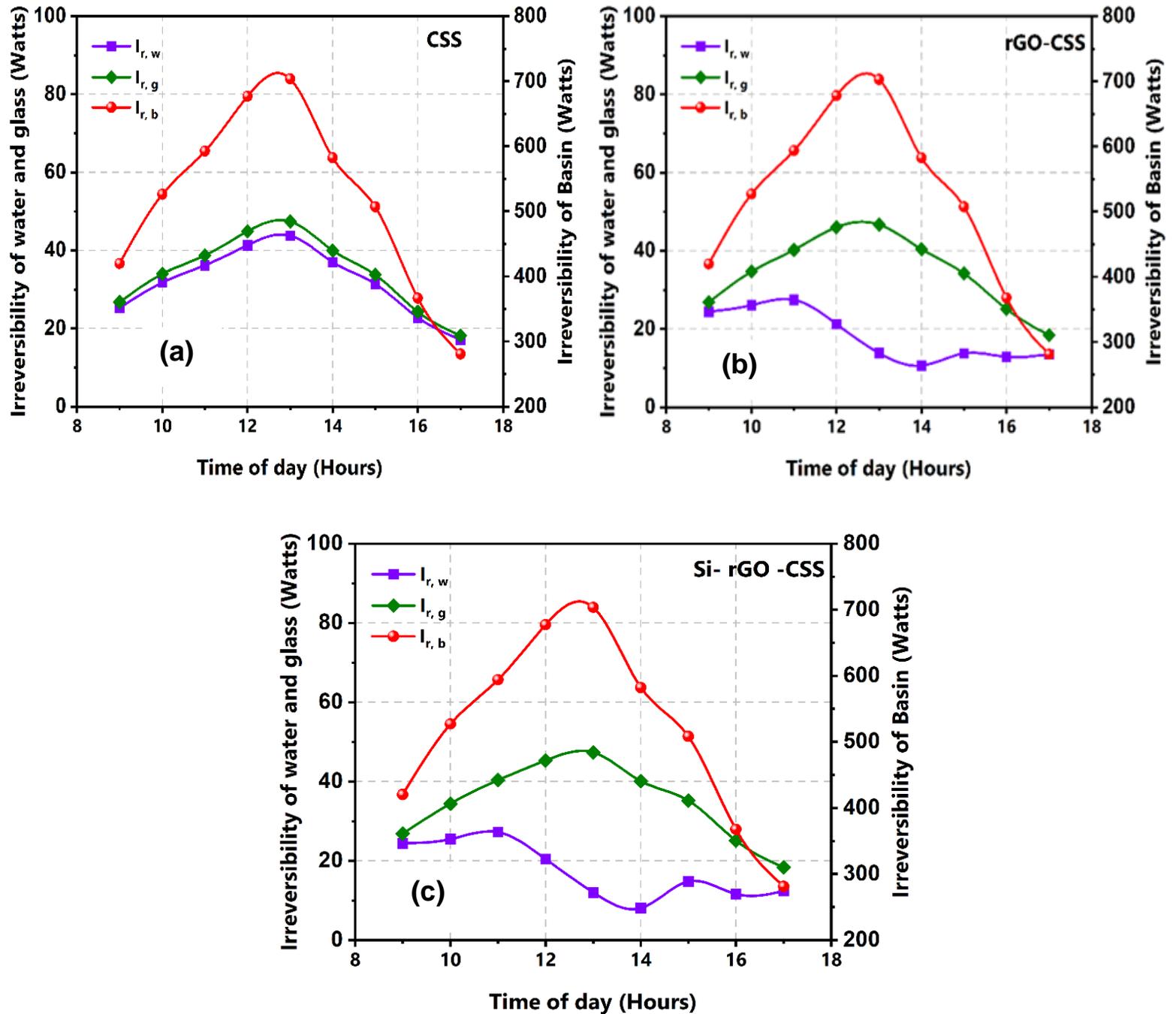

Fig. 18. Irreversibility of water, glass, and basin/absorber of (a) CSS, (b) rGO-CSS, and (c) Si-rGO-CSS as a function of the time of day (daily temperature).

It is concluded from the above outcomes, that the surface modifications of both absorber and condenser provided the optimum enhancement in temperature and leads to improved exergy and energy efficiency of the solar desalination unit.

Daily variation of the irreversibility rates was determining using equations (9-24) and is presented in this section, as follows. Fig. 18 (a-c) illustrates the daily variation in the irreversibility rates for all three SSs. At 1 PM, irreversibility of the basin, water and glass increased and reached a peak and then, slowly decreased and attained its lowest value at 5 PM. It is clear that the CSS basin's rate of irreversibility is much higher than the other two SS components' rates of irreversibility. Similar results for basin irreversibility were stated by Sarhaddi et al. [32]. The absorber's higher rate of irreversibility is owing to the large temperature difference between the basin and the sun, as well as the basin's higher exergy loss rate to the surrounding air compared to the water or glass. The irreversibility of water in the case of the CSS is found to follow a similar curve as the solar radiation, whereas the irreversibility of water decreases in the case of the coated absorber and the dual coated absorber and condensing surface, which could be due to the higher internal evaporation heat transfer coefficient that exists between water and the coated condensing surface. With higher radiation falling on the water surface, continuous evaporation occurs and higher absorption of the solar radiation occurs in the coated absorber that causes a reduction in irreversibility in the water in the case of rGO-CSS and Si-rGO-CSS, respectively. The average rates of irreversibility of water, glass and absorber were 31.84 W, 34.20 W and 517.40 W respectively for the CSS. However, with the absorber coated using rGO (rGO-CSS), the average rates of irreversibility of water, glass and absorber were 18.19 W, 34.71 W and 517.90 W. A similar trend for Si-rGO-CSS was also shown and the average rates of irreversibility of water, glass and absorber were 17.37 W, 34.78 W and 517.97 W, respectively.

5. Physicochemical quality analysis of water

Water quality evaluation and its effective utilization are considered as the most significant features of sustainable water management. Globally, problems with availability of water, its quality and ease of access are ever-present with water insecurity having significances for the physical, mental, and socioeconomic well-being of billions, as highlighted by the Covid-19 pandemic with its public health messaging focus on hand hygiene [37-39]. With the modern passage to decentralization of water management infrastructure and solutions [40], solar desalination at the local scale using SS is considered to be a viable alternative and therefore, the water quality assessment of the product (i.e., the distilled water) should be explored. In this regard, the present work used brackish water as the feed-water and then after distillation, the water physicochemical quality was examined to verify its suitability for drinking purposes.

Test parameters, Unit	'IS 10500-2012' Drinking water		SW, Before distillation	SW, After distillation
	Tolerable limit [13]	Permitted limit [13]		
Total dissolved solids, ppm	500	2000	849	27
pH	6.5 – 8.5	No relaxation	7.2	6.6
Electrical conductivity, µS/cm	-	-	1096	32
Hardness, ppm	200	600	530	13
Turbidity, NTU	1	5	2.1	0.2
Alkalinity, ppm	200	600	390	15
Calcium, ppm	75	200	282	3.1

| Magnesium, ppm | 30 | 100 | 59 | 0.99 |
| Odour | Agreeable | | | Agreeable |

Table 2. Physicochemical quality analysis of water

The brackish feed-water (SW) was collected from the surface–well situated near the Industrial area of Tamilnadu, India. The water quality analysis test was conducted at the standard water testing laboratory in India and the results are presented in Table 2. As can be seen in Table 2, after distillation the distilled water produced from the input SW exhibited excellent physicochemical properties and is suitable for drinking purposes.

6. Cost analysis

The cumulative water yields of the bare CSS, the SS coated with rGO absorber and the SS coated with both rGO absorber and nano-silicon condenser were 2.16 L, 3.03 L and 3.41 L, respectively. Under the experimental test-site (Chennai, India) conditions, the sunshine is available for 80% of the year. Table 3 was presented to determine the total cost of water per liter by using equations 26-33 [41,42] and the cost of water/liter was determined to be 0.0087 $ for the CSS. With the synergetic effect of absorber and condenser coating, the water cost increased slightly (14.9%) but with significant improvement in water productivity (58%).

$$\textbf{T.C}(\textbf{L}) \ = \ \frac{\textbf{Total yearly cost}}{\textbf{Total yearly water yield}} \quad (26)$$

where, T.C (L) is the total cost of freshwater per liter. The total yearly cost can be determined as follows:

$$TYC = YFC + YMOC - YSV \quad (27)$$

where, YFC is the yearly fixed cost, YMOC is the yearly maintenance and operating cost and YSV

is the yearly salvage value, determined as:

$$YFC = RF \times FC \quad (28)$$

where, RF is recovery factor and FC is fixed cost.

$$RF = \frac{(1+i)^n \times i}{(1+i)^n - 1} \quad (29)$$

where, i is the rate of interest/year (10%) and n is desalination unit lifespan (10 years)

$$YMOC = 30\% \times (YFC) \quad (30)$$

$$YSV = SFF \times S \quad (31)$$

where SFF is sinking fund factor and S is the value of salvage.

$$SFF = \frac{i}{(1+i)^n - 1} \quad (32)$$

$$S = 20\% \times (FC) \quad (33)$$

Table 3. Cost of freshwater produced by the different SS

Parameters	Conventional SS	SS with rGO coated absorber	SS with rGO coated absorber + Nano-silicon coated condenser
Fixed cost ($)	57	77	121
Annual fixed cost ($)	9.27	12.53	19.70
Yearly maintenance and operating cost ($)	2.78	3.75	5.90
Total yearly cost ($)	11.34	15.32	24.00

Total annual freshwater Productivity (L/m^2)	1296	1824	2059
Total cost per liter of fresh water, ($/L)	0.0087	0.0084	0.01

7. Comparison of different SS absorber and condenser modification on water productivity

To assess the effect of different coating materials (both i.e., absorber and condenser) on water productivity and thermal performance, the previous published research work is compared with the present work and presented in Table 4.

Table 4. Comparison of yield, thermal performance, and freshwater cost of published work with present work using different absorber/ condenser coating material on absorption material

Author	Experimental site	Absorber coating material	Condenser coating material	Water yield enhancement (%)
Sathyamurthy et al. [11]	Chennai, India	SiO$_2$ (20%)	-	34.3
Kabeel et al. [12]	Chennai, India	TiO$_2$ (0.1%)	-	6.1
Arunkumar et al. [13]	Chennai, India	CuO	-	38.5
		MoO$_3$		28.5
		ZnO		24.3
Thakur et al. [14]	Jaipur, India	Cu	-	33.1
		Al		22.1
		Sn		11.5

Khanmohammadi and Khanjani [16]	Kermanshah Province, Iran	-	Cold-plasma coated glass	25.7
Zanganeh et al. [17]	Fars Province	-	Silicon nanomaterial	20.2
Thakur et al. [43]	Chennai, India	MXene	-	12.5%
Thakur et al. [44]	Chennai, India	Activated carbon	-	39.3%
Present work	**Chennai, India**	**rGO (10%)**	**Nano-Si**	**58**

The augmentation in the water yield has changed significantly with different kinds of coating material. The majority of research has used oxide nanoparticles in the absorber coating and have improved the water yield, whereas only a very few studies have modified the condenser coating. However, no research has reported the effect of modifying both surface coatings, i.e., condenser and absorber. From Table 4, it can be seen that the synergistic effect of absorber and condenser coating on the SS significantly augmented the water yield and a maximum enhancement in the water yield of 58 % was found in the present case.

8. Conclusion

A modified SS with absorber and condenser coating was investigated experimentally and compared with the water purification performance of a conventional SS. Two different combinations were assessed as modifications of the solar still, namely: rGO-CSS with the solar absorber coated using BP supplemented with 10 wt. % reduced graphene oxide (rGO) along with a conventional glass cover, and Si-rGO-CSS in which the glass cover was coated using nano-silicon and the absorber was coated with BP in which 10 wt. % rGO was dispersed. All three cases

(conventional, coated absorber, and both absorber & glass coated) were examined under identical ambient conditions on the same days in Chennai, India. The modified solar desalination units demonstrated their feasibility and augmented the overall system performance, generating distilled water which is suitable for drinking. The developed desalination units were assessed from different viewpoints: water yield and effect of condenser coating on water droplet movement and water yield, thermal performance including energy efficiency and instantaneous gain in energy efficiency, exergy efficiency and the irreversibility of different components, and finally the water cost and physicochemical quality analysis. The following major conclusions are drawn from the present study:

- The conventional glass condenser exhibited hydrophilic behavior and hindered the smooth movement of water droplets from the inclined condenser, leading to a prolonged time of 120 $\pm$ 0.1 seconds for water droplets to complete their glide from the center to the bottom of the glass. However, nano-silicon coated glass exhibited hydrophobic behavior and significantly improved the water droplet movement such that the water droplet could glide from the center to the bottom of the glass in just 25 $\pm$ 0.1 seconds.

- The modified desalination units showed substantially augmented water yields compared to the conventional SS, with yields increased by 58 % and 40 %, for the Si-rGO-CSS and rGO-CSS, respectively, due to the exceptional solar-absorption of rGO along with the drop-wise condensation behavior and faster droplet movement on the nano-silicon coated glass.

- The system's overall thermal performance improved also, whereby the Si-rGO-CSS improved the average full-day energy efficiency by (37 % and 12.3 %), and average full-day exergy efficiency by (112 % and 13.2 %) compared to the CSS (uncoated) and rGO-CSS (condenser-only coated) stills, respectively. In addition, non-linear characteristic equations were found to

be better than linear characteristic equations for determining the instantaneous gain in energy efficiency for the coated SS with constant water depths.

- Irreversibility analysis of the water, glass and absorber demonstrated the highest rate of irreversibility by the absorber in all three SS owing to the temperature difference between the basin/absorber and the sun, along with a high exergy loss rate of the basin to the surroundings. It is recommended to improve the basin/absorber design along with the glass cover material.

- The freshwater cost per liter for the dual-modified still (Si-rGO-CSS) was 0.01 \$. Water physicochemical quality analysis before and after desalination revealed that the quality of water was significantly enriched after evaporation and it was found to be fully compliant with the requirements and prescribed limits of the drinking water quality 'IS 10500-2012' standard.

- It is concluded that the synergetic effect of coating the absorber with highly conductive materials and coating the condenser with a hydrophobic coating will pave the way towards development of sustainable and energy efficient solar desalination units for converting brackish / saline water into clean potable water, especially for rural populations.

Abbreviations

BP   :   Black paint

CSS   :   Conventional solar still

NTU   :   Nephelometric turbidity units

rGO   :   Reduced graphene oxide

rGO-CSS   :   Solar still with rGO coated absorber

Si-rGO-CSS   :   Solar still with nano-silicon coated glass cover and rGO coated absorber

SSs : Solar stills

SW : Surface–well brackish feed-water

WCA : Water contact angle

Declaration of competing interest

The authors declare that they have no known competing financial interests or personal relationships that could have appeared to influence the work reported in this paper.

References

1. World Water Assessment Programme (Nations Unies), The United Nations World Water Development Report 2018 (United Nations Educational, Scientific and Cultural Organization, New York, United States) www.unwater.org/publications/world-water-development-report-2018/. (2018).

2. T. Yan, G. Xie, L. Sun, M. Du, H. Liu, Experimental investigation on a two-effect tubular solar still operating under vacuum conditions, Desalination 468 (2019),114057.

3. U. Atikol, H.S. Aybar, Estimation of water production cost in the feasibility analysis of RO systems, Desalination 184 (2005) 253-258.

4. M. Ahmed, A. Arakel, D. Hoey, M.R. Thumarukudy, M.F.A. Goosen, M. Al-Haddabi, et al., Feasibility of salt production from inland RO desalination plant reject brine: a case study, Desalination 158 (2003/08/01/2003) 109-117.

5. S.A. Kalogirou, Seawater desalination using renewable energy sources, Prog. Energy Combust. Sci. 31 (2005) 242–281.

6. Thakur, A.K., Sathyamurthy, R. Improving the potable water generation through tubular solar still using eggshell powder (bio-based energy source) as a natural energy storage material — an experimental approach. Environ Sci Pollut Res (2022). https://doi.org/10.1007/s11356-022-18906-8

7. Thakur AK, Sharshir SW, Ma Z, Thirugnanasambantham A, Christopher SS, Vikram MP, et al. Performance amelioration of single basin solar still integrated with V- type concentrator: energy, exergy, and economic analysis. Environ. Sci. Pollut. Res. 2021;28:3406–20.

8. Thakur AK, Sathyamurthy R, Velraj R, Lynch I, Saidur R, Pandey AK, Sharshir SW et al., Sea-water desalination using a desalting unit integrated with a parabolic trough collector and activated carbon pellets as energy storage medium. Desalination 516 (2021) 115217.

9. S. Bisht, G.S. Dhindsa, S.S. Sehgal, Augmentation of diurnal and nocturnal distillate of solar still having wicks in the basin and integrated with solar pond, Materials Today: Proceedings 33 (2020) 1615–1619.

10. K. Elmaadawy, A.W. Kandeal, A. Khalil, M.R. Elkadeem, B. Liu, S.W. Sharshir, Performance improvement of double slope solar still via combinations of low cost materials integrated with glass cooling, Desalination. 500 (2021), 114856, https://doi.org/10.1016/j.desal.2020.114856.

11. R. Sathyamurthy, A.E. Kabeel, M. Balasubramanian, M. Devarajan, S.W. Sharshir, A.M. Manokar, Experimental study on enhancing the yield from stepped solar still coated using fumed silica nanoparticle in black paint, Mater. Lett. 272 (2020), 127873.

12. Kabeel AE, Sathyamurthy Ravishankar, Sharshir Swellam W, Muthumanokar A, Hitesh Panchal N, Prakash C, et al. Effect of water depth on a novel absorber plate of pyramid solar

still coated with TiO2 nano black paint. J Clean Prod 2019; 213 (185–191). https://doi.org/10.1016/j.jclepro.2018.12.185.

13. Arunkumar, T., Murugesan, D., Viswanathan, C. et al. Effect of CuO, MoO3 and ZnO nanomaterial coated absorbers for clean water production. SN Appl. Sci. 2, 1709 (2020). https://doi.org/10.1007/s42452-020-03504

14. A.K. Thakur, R. Sathyamurthy, S.W. Sharshir, A.E. Kabeel, A.M. Manokar, W. Zhao, An experimental investigation of a water desalination unit using different microparticle-coated absorber plate: yield, thermal, economic, and environmental assessments, Environ. Sci. Pollut. Res. Int. (2021), https://doi.org/10.1007/s11356-021-12837-6.

15. Arani, R.P., Sathyamurthy, R., Chamkha, A. et al. Effect of fins and silicon dioxide nanoparticle black paint on the absorber plate for augmenting yield from tubular solar still. Environ Sci Pollut Res 28, 35102–35112 (2021). https://doi.org/10.1007/s11356-021-13126-y

16. Khanmohammadi, S and Khanjani, S. Experimental study to improve the performance of solar still desalination by hydrophobic condensation surface using cold plasma technology. Sustainable Energy Technologies and Assessments 45 (2021) 101129. https://doi.org/10.1016/j.seta.2021.101129

17. P. Zanganeh, A.S. Goharrizi, S. Ayatollahi, M. Feilizadeh, Nano-coated condensation surfaces enhanced the productivity of the single-slope solar still by changing the condensation mechanism, J. Clean. Prod. 265 (2020), 121758.

18. Yang J, Jia Y, Bing N, Wang L, Xie H, Yu W. Reduced graphene oxide and zirconium carbide co-modified melamine sponge / paraffin wax composites as new form-stable phase change materials for photothermal energy conversion and storage. Appl Therm Eng 2019;163. https://doi.org/10.1016/j. applthermaleng.2019.114412.

19. N. El-Shafai, M. E. El-Khouly, M. El-Kemary, M. Ramadan, I. Eldesoukey, and M. Masoud, "Graphene oxide decorated with zinc oxide nanoflower, silver and titanium dioxide nanoparticles: fabrication, characterization, DNA interaction, and antibacterial activity," RSC advances, vol. 9, pp. 3704-3714, 2019.

20. N. M. El-Shafai, M. M. Abdelfatah, M. E. El-Khouly, I. M. El-Mehasseb, A. El-Shaer, M. S. Ramadan, M. S. Masoud, and M. A. El-Kemary, "Magnetite nano-spherical quantum dots decorated graphene oxide nano sheet (GO@ Fe3O4): Electrochemical properties and applications for removal heavy metals, pesticide and solar cell," Applied Surface Science, vol. 506, p. 144896, 2020.

21. M. Kędzierski, P. Jankowski, G. Jaworska, and A. Niska, "Graphite oxide as an intumescent flame retardant for polystyrene," Polimery, vol. 57, pp. 347-353, 2012.

22. L.-Y. Meng and S.-J. Park, "Preparation and characterization of reduced graphene nanosheets via pre-exfoliation of graphite flakes," Bull. Korean Chem. Soc, vol. 33, pp. 209-214, 2012.

23. X. Cheng, H. Liu, Q. Chen, J. Li, and P. Wang, "Preparation of graphene film decorated TiO2 nano-tube array photoelectrode and its enhanced visible light photocatalytic mechanism," Carbon, vol. 66, pp. 450-458, 2014.

24. A.K. Thakur, R. Sathyamurthy, R. Velraj, R. Saidur, J.Y. Hwang, Augmented performance of solar desalination unit by utilization of nano-silicon coated glass cover for promoting drop-wise condensation, Desalination 515 (2021), 115191, https://doi.org/10.1016/j.desal.2021.115191.

25. Amjad, R.J., Sahar, M.R., Ghoshal, S.K., Dousti, M.R., Riaz, S., Samavati, A.R., Jamaludin, M.A. and Naseem, S., 2013. Plasmon-enhanced upconversion fluorescence in Er3+: Ag phosphate glass: the effect of heat treatment. Chinese Physics Letters, 30(2), p.027301.

26. Ge, M., Rong, J., Fang, X., Zhang, A., Lu, Y. and Zhou, C., 2013. Scalable preparation of porous silicon nanoparticles and their application for lithium-ion battery anodes. Nano Research, 6(3), pp.174-181.

27. Alaa H. Salah, Gasser E. Hassan, Hassan Fath, Mohamed Elhelw, Samy Elsherbiny, Analytical investigation of different operational scenarios of a novel greenhouse combined with solar stills, Appl. Thermal Eng. 122 (2017) 297–310.

28. Richard Petela, Exergy of undiluted thermal radiation, Solar Energy 74 (6) (2003) 469–488.

29. Emrah Deniz, Serkan Çınar, Energy, exergy, economic and environmental (4E) analysis of a solar desalination system with humidification-dehumidification, Energy Convers. Manag. 126 (2016) 12–19.

30. Kotas TJ. The exergy method of thermal plant analysis. Elsevier; 2013.

31. Yazdanpanahi J, Sarhaddi F, Adeli MM. Experimental investigation of exergy efficiency of a solar photovoltaic thermal (PVT) water collector based on exergy losses. Sol Energy 2015;118:197–208.

32. Sarhaddi, F., Tabrizi, F.F., Zoori, H.A. and Mousavi, S.A.H.S., 2017. Comparative study of two weir type cascade solar stills with and without PCM storage using energy and exergy analysis. Energy Conversion and Management, 133, pp.97-109.

33. Dhivagar, R., Mohanraj, M., Hidouri, K. and Belyayev, Y., 2021. Energy, exergy, economic and enviro-economic (4E) analysis of gravel coarse aggregate sensible heat storage-assisted single-slope solar still. Journal of Thermal Analysis and Calorimetry, 145(2), pp.475-494.

34. Wenzel, R. N. Resistance of solid surfaces to wetting by water. Ind. Eng. Chem. https://doi.org/10.1021/ie50320a024 (1936).

35. Bayati, M. R.; Zargar, H. R.; Talimian, A.; Ziaee, A.; Molaei, R. Characterization of Al2O3–TiO2 Nano Porous Solar Absorbers Derived via MAO/Sol-Gel Hybrid Process. Surf. Coat. Technol. 2010, 205, 2483–2489.

36. Dev, R and Tiwari, G N. Characteristic equation of a hybrid (PV-T) active solar still. Desalination 254 (2010) 126–137.

37. Hannah, D.M., Lynch, I., Mao, F. et al. Water and sanitation for all in a pandemic. Nat Sustain 3, 773–775 (2020). https://doi.org/10.1038/s41893-020-0593-7

38. A.K. Thakur, R. Sathyamurthy et al., A case study of SARS-CoV-2 transmission behavior in a severely air-polluted city (Delhi, India) and the potential usage of graphene based materials for filtering air-pollutants and controlling/monitoring the COVID-19 pandemic. Environ. Sci.: Processes Impacts, 2021,23, 923-946. https://doi.org/10.1039/D1EM00034A

39. A.K. Thakur, R. Sathyamurthy et al., Secondary transmission of SARS-CoV-2 through wastewater: Concerns and tactics for treatment to effectively control the pandemic. Journal of Environmental Management 290 (2021) 112668. https://doi.org/10.1016/j.jenvman.2021.112668

40. Leigh NG, Lee H. Sustainable and Resilient Urban Water Systems: The Role of Decentralization and Planning. Sustainability. 2019; 11(3):918. https://doi.org/10.3390/su11030918 \

41. H.E.S. Fath, M. El-Samanoudy, K. Fahmy, A. Hassabou, Thermal-economic analysis and comparison between pyramid-shaped and single-slope solar still configurations, Desalination, 159 (2003) 69-79.

42. Sharshir, S.W., Eltawil, M.A., Algazzar, A.M., Sathyamurthy, R. and Kandeal, A.W., 2020. Performance enhancement of stepped double slope solar still by using nanoparticles and linen wicks: energy, exergy and economic analysis. Applied Thermal Engineering, 174, p.115278.

43. Thakur, A.K., Sathyamurthy, R., Saidur, R., Velraj, R., Lynch, I. and Aslfattahi, N., 2022. Exploring the potential of MXene-based advanced solar-absorber in improving the performance and efficiency of a solar-desalination unit for brackish water purification. Desalination, 526, p.115521.

44. Thakur AK, Sathyamurthy R, Velraj R, Saidur R, Lynch I, Venkatesh R, Kumar PG, Kim SC, Sillanpää M. A novel solar absorber using activated carbon nanoparticles synthesized from bio-waste for the performance improvement of solar desalination unit. Desalination. 2022 Apr 1;527:115564.